THE ASTROPHYSICAL JOURNAL, 964:71 (35pp), 2024 March 20
© 2024. The Author(s). Published by the American Astronomical Society.
OPEN ACCESS

https://doi.org/10.3847/1538-4357/ad1ee4

CrossMark

The Cosmos in Its Infancy: JADES Galaxy Candidates at $z > 8$ in GOODS-S and GOODS-N

Kevin N. Hainline[1] , Benjamin D. Johnson[2] , Brant Robertson[3] , Sandro Tacchella[4,5] , Jakob M. Helton[1] , Fengwu Sun[1] ,
Daniel J. Eisenstein[2] , Charlotte Simmonds[4,5] , Michael W. Topping[1] , Lily Whitler[1] , Christopher N. A. Willmer[1] ,
Marcia Rieke[1] , Katherine A. Suess[6,7] , Raphael E. Hviding[1] , Alex J. Cameron[8] , Stacey Alberts[1] , William M. Baker[4,5] ,
Stefi Baum[9] , Rachana Bhatawdekar[10,11] , Nina Bonaventura[1,12,13] , Kristan Boyett[14,15] , Andrew J. Bunker[8] ,
Stefano Carniani[16] , Stephane Charlot[17] , Jacopo Chevallard[8] , Zuyi Chen[1] , Mirko Curti[4,5,18] , Emma Curtis-Lake[19] ,
Francesco D'Eugenio[4,5] , Eiichi Egami[1] , Ryan Endsley[20] , Ryan Hausen[21] , Zhiyuan Ji[1] , Tobias J. Looser[4,5] ,
Jianwei Lyu[1] , Roberto Maiolino[4,5,22] , Erica Nelson[23] , Dávid Puskás[4,5] , Tim Rawle[10] , Lester Sandles[4,5] ,
Aayush Saxena[8,22] , Renske Smit[24] , Daniel P. Stark[1] , Christina C. Williams[25] , Chris Willott[26] , and Joris Witstok[4,5]
[1] Steward Observatory, University of Arizona, 933 N. Cherry Avenue, Tucson, AZ 85721, USA
[2] Center for Astrophysics | Harvard & Smithsonian, 60 Garden Street, Cambridge, MA 02138, USA
[3] Department of Astronomy and Astrophysics, University of California, Santa Cruz, 1156 High Street, Santa Cruz, CA 96054, USA
[4] Kavli Institute for Cosmology, University of Cambridge, Madingley Road, Cambridge, CB3 0HA, UK
[5] Cavendish Laboratory, University of Cambridge, 19 JJ Thomson Avenue, Cambridge, CB3 0HE, UK
[6] Department of Astronomy and Astrophysics, University of California, Santa Cruz, 1156 High Street, Santa Cruz, CA 95064, USA
[7] Kavli Institute for Particle Astrophysics and Cosmology and Department of Physics, Stanford University, Stanford, CA 94305, USA
[8] Department of Physics, University of Oxford, Denys Wilkinson Building, Keble Road, Oxford, OX1 3RH, UK
[9] Department of Physics and Astronomy, University of Manitoba, Winnipeg, MB, R3T 2N2, Canada
[10] European Space Agency (ESA), European Space Astronomy Centre (ESAC), Camino Bajo del Castillo s/n, 28692 Villanueva de la Cañada, Madrid, Spain
[11] European Space Agency, ESA/ESTEC, Keplerlaan 1, 2201 AZ Noordwijk, The Netherlands
[12] Cosmic Dawn Center (DAWN), Copenhagen, Denmark
[13] Niels Bohr Institute, University of Copenhagen, Jagtvej 128, DK-2200, Copenhagen, Denmark
[14] School of Physics, University of Melbourne, Parkville, VIC 3010, Australia
[15] ARC Centre of Excellence for All Sky Astrophysics in 3 Dimensions (ASTRO 3D), Australia
[16] Scuola Normale Superiore, Piazza dei Cavalieri 7, I-56126 Pisa, Italy
[17] Sorbonne Université, CNRS, UMR 7095, Institut d'Astrophysique de Paris, 98 bis bd Arago, 75014 Paris, France
[18] European Southern Observatory, Karl-Schwarzschild-Strasse 2, 85748 Garching, Germany
[19] Centre for Astrophysics Research, Department of Physics, Astronomy and Mathematics, University of Hertfordshire, Hatfield, AL10 9AB, UK
[20] Department of Astronomy, University of Texas, Austin, TX 78712, USA
[21] Department of Physics and Astronomy, The Johns Hopkins University, 3400 N. Charles St. Baltimore, MD 21218, USA
[22] Department of Physics and Astronomy, University College London, Gower Street, London, WC1E 6BT, UK
[23] Department for Astrophysical and Planetary Science, University of Colorado, Boulder, CO 80309, USA
[24] Astrophysics Research Institute, Liverpool John Moores University, 146 Brownlow Hill, Liverpool, L3 5RF, UK
[25] NSF's National Optical-Infrared Astronomy Research Laboratory, 950 North Cherry Avenue, Tucson, AZ 85719, USA
[26] NRC Herzberg, 5071 West Saanich Rd, Victoria, BC, V9E 2E7, Canada
Received 2023 June 3; revised 2023 December 29; accepted 2024 January 7; published 2024 March 18

Abstract

We present a catalog of 717 candidate galaxies at $z > 8$ selected from 125 square arcmin of NIRCam imaging as part of the JWST Advanced Deep Extragalactic Survey (JADES). We combine the full JADES imaging data set with data from the JWST Extragalactic Medium Survey and First Reionization Epoch Spectroscopic COmplete Survey (FRESCO) along with extremely deep existing observations from Hubble Space Telescope (HST)/ Advanced Camera for Surveys (ACS) for a final filter set that includes 15 JWST/NIRCam filters and five HST/ ACS filters. The high-redshift galaxy candidates were selected from their estimated photometric redshifts calculated using a template-fitting approach, followed by visual inspection from seven independent reviewers. We explore these candidates in detail, highlighting interesting resolved or extended sources, sources with very red long-wavelength slopes, and our highest-redshift candidates, which extend to $z_{\rm phot} \sim 18$. Over 93% of the sources are newly identified from our deep JADES imaging, including 31 new galaxy candidates at $z_{\rm phot} > 12$. We also investigate potential contamination by stellar objects, and do not find strong evidence from spectral energy distribution fitting that these faint high-redshift galaxy candidates are low-mass stars. Using 42 sources in our sample with measured spectroscopic redshifts from NIRSpec and FRESCO, we find excellent agreement to our photometric redshift estimates, with no catastrophic outliers and an average difference of $\langle \Delta z = z_{\rm phot} - z_{\rm spec} \rangle = 0.26$. These sources comprise one of the most robust samples for probing the early buildup of galaxies within the first few hundred million years of the Universe's history.

Unified Astronomy Thesaurus concepts: Extragalactic astronomy (506); Redshift surveys (1378); James Webb Space Telescope (2291); High-redshift galaxies (734); Galaxies (573)

Original content from this work may be used under the terms of the Creative Commons Attribution 4.0 licence. Any further distribution of this work must maintain attribution to the author(s) and the title of the work, journal citation and DOI.

1

1. Introduction

The earliest galaxies that appeared from the Cosmic Dark Ages fundamentally changed the Universe. For hundreds of millions of years after recombination, the decoupling of matter and radiation, the Universe's baryon content consisted of predominantly neutral hydrogen that was gravitationally pooling and collecting, pulled by early dark matter halos. Eventually, these massive clouds collapsed and formed the first stars, which gave off energetic ultraviolet (UV) radiation, ionizing the neutral hydrogen medium throughout the Universe. Reionization is thought to have taken place across the the first billion years after the Big Bang, but exactly how this process occurred, and more specifically what types of galaxies were responsible for this phase transition, has been an active area of research for decades (Barkana & Loeb 2001; Stark 2016; Dayal & Ferrara 2018; Finkelstein et al. 2019; Ouchi et al. 2020; Robertson et al. 2023). Observations of early galaxies offer us a vital insight into the first stages of galaxy formation and evolution, and help us understand the emergence of the elements heavier than helium. To aid in understanding these distant sources, in this paper we present a sample of 717 galaxies and candidate galaxies with spectroscopic and photometric redshifts corresponding to the first 200–600 Myr after the Big Bang and describe their selection and properties.

To explore the very early Universe, researchers search for galaxies at increasingly high redshifts using deep observations from space. One of the pioneering early Universe surveys was the Hubble Space Telescope (HST) Deep Field project (HDF; Williams et al. 1996), a set of observations at wavelengths spanning the near-ultraviolet to near-infrared (near-IR). These data provided an opportunity to explore galaxy evolution out to $z = 4-5$ (Madau et al. 1996). Following the success of the HDF, the next decades were spent observing multiple deep fields down to unprecedented observational depths of 30 mag (AB) at optical and near-IR wavelengths. These surveys included the Hubble Ultra-Deep Field (HUDF; Beckwith et al. 2006), HUDF09 (Bouwens et al. 2011b), HUDF12 (Ellis et al. 2013; Koekemoer et al. 2013), the UVUDF (Teplitz et al. 2013), the HST Great Observatories Origins Deep Survey (GOODS; Giavalisco et al. 2004), the Cosmological Evolution Survey (COSMOS; Scoville et al. 2007), and the Cosmic Assembly Near-infrared Deep Extragalactic Legacy Survey (CANDELS; Grogin et al. 2011; Koekemoer et al. 2011). The Brightest of Reionizing Galaxy survey (BoRG; Trenti et al. 2011) was a campaign to search for bright high-redshift galaxies across a wide (274 square arcmin) but relatively shallow area. Researchers hoping to target fainter galaxies also focused on lensing clusters, leading to the Cluster Lensing and Supernova Survey with Hubble (CLASH; Postman et al. 2012), the Hubble Frontier Fields (HFF; Lotz et al. 2017), and the Reionization Lensing Cluster Survey (RELICS;f Coe et al. 2019).

It has therefore been exciting to see the fruits of these observations: the discovery of many thousands of galaxies at $z > 4$ (Bunker et al. 2004, 2010; Bouwens et al. 2011a, 2015, 2022; Lorenzoni et al. 2011; Ellis et al. 2013; McLure et al. 2013; Oesch et al. 2013, 2014, 2018; Schenker et al. 2013; Finkelstein et al. 2015, 2023; Ishigaki et al. 2015; Harikane et al. 2016; McLeod et al. 2016; Morishita et al. 2018; Bridge et al. 2019; Rojas-Ruiz et al. 2020; Bagley et al. 2024). While these sources have been found through multiple methods, the primary method of high-redshift galaxy selection relies on photometry alone. Neutral hydrogen within, surrounding, and between distant galaxies serves to absorb UV radiation, leading

to what is commonly referred to as the "Lyman break" in the spectral energy distribution (SED) at 912 Å. At redshifts above $z > 5$, the increasingly neutral hydrogen in the Universe results in Lyα forest absorption between 912 and 1216 Å, and sources at these redshifts are more commonly known as "Lyα break" or "Lyα dropout" galaxies. By identifying galaxies where the Lyman break and Lyα break fell between two adjacent filters at a given redshift, these sources could be selected in large quantities, as done initially in Guhathakurta et al. (1990) and Steidel & Hamilton (1992). A similar approach involves fitting galaxy photometry to simulated or observed galaxy SEDs, a method that utilizes more data than pure color selection (Koo 1985, 1999; Gwyn & Hartwick 1996; Lanzetta et al. 1996; Pello et al. 1996; Bolzonella et al. 2000). These results require accurate template sets that span the full color space of the photometric data, and include the effects of both dust extinction and intergalactic medium (IGM) absorption. This template-fitting procedure is uncertain at high redshifts given the current lack of UV and optical SEDs for galaxies in the early Universe (for a review of selection methods for finding high-redshift galaxies, see Stern & Spinrad 1999; Giavalisco 2002; Dunlop 2013; Stark 2016).

While both galaxy selection techniques have been used to find galaxies out to $z \sim 10$ with HST, the reddest filter on the telescope's Wide-Field Camera 3 (WFC3/IR) is at 1.6 μm, such that potential galaxies at higher redshifts would have their Lyα break shifted out of the wavelength range of the instrument. Exploring the evolution of galaxies at earlier times was limited by the availability of deep, high-resolution near- and mid-infrared (mid-IR) observations. This changed with the launch of the JWST in late 2021, an observatory carrying a suite of sensitive IR instruments behind a 6.5 m primary mirror. The instruments include NIRCam (Rieke et al. 2005), a high-resolution camera operating at 0.7–5.0 μm across a 9.7 square arcmin field of view, and NIRSpec (Jakobsen et al. 2022), a spectrograph operating at similar wavelengths with a unique multi-object shutter array capable of obtaining spectra at multiple resolutions.

In the first year of JWST science, researchers have identified scores of candidate high-redshift galaxies at $z > 8$ (Castellano et al. 2022; Naidu et al. 2022; Adams et al. 2023; Atek et al. 2023; Austin et al. 2023; Donnan et al. 2023; Finkelstein et al. 2023; Harikane et al. 2023; Leethochawalit et al. 2023; Morishita et al. 2023; Pérez-González et al. 2023; Whitler et al. 2023; Yan et al. 2023). Some of these sources have been spectroscopically confirmed at $z > 8$ (Arrabal Haro et al. 2023a, 2023b), demonstrating the efficacy of using NIRCam for early Universe observations. It should be noted, however, that this is an imperfect science—Arrabal Haro et al. (2023a) describe how the early bright $z \sim 16$ candidate CEERS-93316 was spectroscopically found to be at $z_{spec} = 4.9$ with strong line emission and dust obscuration simulating the colors of a distant galaxy, a possibility discussed in Naidu et al. (2022) and Zavala et al. (2023).

One of the largest JWST Cycle 1 extragalactic surveys by time allocation is the JWST Advanced Deep Extragalactic Survey (JADES; Rieke 2023), a Guaranteed Time Observations (GTO) program that will eventually encompass 770 hr of observations from three of the telescope's instruments: NIRCam, NIRSpec, and the mid-IR instrument, MIRI. These data, which focus on the GOODS-S and GOODS-N regions of the sky, are ideal for finding and understanding the most distant galaxies through imaging and follow-up spectroscopy. Because the JADES target regions have been observed by multiple

telescopes and instruments across the electromagnetic spectrum, there is a rich quantity of ancillary data for comparing with JWST images and spectroscopy.

Early JADES observations resulted in the discovery of the highest-redshift spectroscopically confirmed galaxy thus far, JADES-GS-z13-0 ($z_{\rm spec} = 13.20^{+0.04}_{-0.07}$; Curtis-Lake et al. 2023; Robertson et al. 2023). Because of NIRCam's wavelength range and dichroic offering simultaneous short-wavelength (0.7–2.3 μm) and long-wavelength (2.4–5.0 μm) images, these and other high-redshift candidates are detected in multiple bands at wavelengths longward of the Lyα break. The high-redshift galaxies that can be observed thanks to the wavelength coverage of JWST are vital for exploring the potential downturn in the number density of ultra-high-redshift ($z \gtrsim 10$) galaxies previously predicted by HST observations alone (Oesch et al. 2018).

In this study, we present the results of a search through the first year of JADES NIRCam imaging of the GOODS-S and GOODS-N regions for galaxy candidates at $z > 8$, where we combine the deepest HST optical and near-IR observations with JADES NIRCam data taken across 10 filters. These data are supplemented by medium-band JWST imaging in five additional filters from both the publicly available JWST Extragalactic Medium Survey (JEMS; Williams et al. 2023b) and First Reionization Epoch Spectroscopic COmplete Survey (FRESCO; Oesch et al. 2023) programs. We perform template fitting in order to select candidate high-redshift candidates, capitalizing on the large number of filters at wavelengths longer than 2 μm. Because of both the unparalleled HST coverage and the mixture of medium and wide NIRCam filters present in the JADES data, these data currently represent the best opportunity for uncovering galaxies at $z > 8$ with minimal low-redshift interlopers. The deepest portions of the JADES data set probe down to 5σ depths of 2.17 nJy (30.6 mag AB) at 2.7 μm, currently deeper than the other similar JWST extragalactic fields studied in the literature. In addition, because of the FRESCO grism spectra and the JADES NIRSpec spectroscopy, we also have a number of spectroscopic redshifts for these sources confirming their selection, providing constraints on the accuracy of photometric redshifts for galaxies in the early Universe.

The structure of this paper is as follows. We begin by introducing the JADES data set used in this study, and we discuss our data reduction and photometric and spectroscopic measurements in Section 2. In Section 3, we describe how we estimate photometric redshifts and, from these results, select candidate galaxies at $z > 8$. We then spend the bulk of this study exploring the resulting sample in Section 4, separating the objects into three bins: $z = 8-10$ (Section 4.1), $z = 10-12$ (Section 4.2), and $z > 12$ (Section 4.3). We then consider candidate galaxies that fall out of our primary selection either because of their template fits (Section 4.4) or their proximity to brighter sources (Section 4.5). We also discuss the possibility of these sources being low-mass stars (Section 4.6), describe which candidates have been included in samples previous to this study (Section 4.7), and explore the impact of different galaxy template sets for photometric redshifts (Section 4.8). Finally, we examine the selection and further properties of these sources in Section 5 and conclude in Section 6. Throughout this paper, we assume a Planck Collaboration et al. (2020) cosmology with $H_0 = 67.4$ km s^{-1} Mpc^{-1}, $\Omega_{\rm M} = 0.315$, and $\Omega_{\Lambda} = 0.685$. All magnitudes are provided using the AB magnitude system (Oke 1974; Oke & Gunn 1983).

2. JADES Imaging and Photometry

JADES is a joint GTO program between the NIRCam and NIRSpec extragalactic GTO teams that consists of NIRCam imaging, NIRSpec spectroscopy, and MIRI imaging across the GOODS-S (R.A. = 53.126 deg, decl. = −27.802 deg) and GOODS-N (R.A. = 189.229, decl. = +62.238 deg) (Giavalisco et al. 2004) fields. In this section, we describe the Cycle 1 JADES observations taken as of 2023 February 8, the data reduction, and the measurement of fluxes and spectroscopic redshifts. The full description of these observations is provided in Eisenstein et al. (2023a).

2.1. Observations

In this paper, we will discuss galaxy candidates selected from the NIRCam imaging in both GOODS-S, with observations taken on UT 2022 February 29 through 2022 October 10 (Program 1180, PI: Eisenstein), and GOODS-N, with observations taken on UT 2023 February 3 through 2023 February 7 (Program 1181, PI: Eisenstein). In addition, a set of NIRCam parallels (9.8 square arcmin each) were observed during NIRSpec observation PID 1210 (PI: Ferruit) on UT 2022 October 20 to 2022 October 24 within and southwest of the JADES Medium footprint in GOODS-S. Another set of NIRCam observations (9.8 square arcmin) parallel to NIRSpec PID 1286 (PI: Ferruit) were observed on UT 2023 January 12 to 2023 January 13 to the northwest (NW) of the JADES Deep footprint in GOODS-S. These data were partly presented in both Robertson et al. (2023) as well as Tacchella et al. (2023), although here we combine the full suite of JADES data observed as of 2023 February 8.

The total current survey area of the JADES GOODS-S is 67 square arcmin, with 27 square arcmin for the JADES Deep program and 40 square arcmin for the JADES Medium program. The filters used for JADES Deep are NIRCam F090W, F115W, F150W, F200W, F277W, F335M, F356W, F410M, and F444W ($\lambda = 0.8$–5.0 μm), while JADES Medium uses the same filters without F335M. For the 1286 parallel, the JADES observations include the F070W filter.

The total current area of the NIRCam GOODS-N program is 58 square arcmin. The NIRCam filters observed for GOODS-N are F090W, F115W, F150W, F200W, F277W, F335M, F356W, F410M, and F444W ($\lambda = 0.8$–5.0 μm). The GOODS-N observations are separated into two portions: the NW portion, which covers 30.4 square arcmin, and a southeast (SE) portion, which covers 27.6 square arcmin. The NW portion was taken under PID 1181 (PI: Eisenstein) with NIRCam as the prime instrument and MIRI in parallel, while the southwest (SW) portion was taken as part of the same program with NIRSpec as prime and NIRCam in parallel.

We also include observations taken for JEMS (Williams et al. 2023b). These data, which are part of program PID 1963 (PIs: Williams, Tacchella, Maseda) were taken on UT 2022 October 12. For this study, we use the NIRCam data from JEMS, which cover the Ultra-Deep Field (UDF; Beckwith et al. 2006) by the NIRCam A module, with the NIRCam B module to the SW, spanning the JADES Deep and Medium portions, for a total area of 10.1 square arcmin. The NIRCam observations in the JEMS survey were taken with the F182M, F210M, F430M, F460M, and F480M filters (Williams et al. 2023b).

We also supplement our observations with NIRCam data from FRESCO (PID 1895, PI: Oesch). While nominally a

NIRCam grism survey across GOODS-S and GOODS-N, we use the FRESCO F182M, F210M, and F444W imaging of GOODS-S and GOODS-N to supplement the filters available in JADES. The FRESCO area extends beyond the JADES Deep and Medium regions, and we do not select galaxies in this region due to the lack of NIRCam filter coverage afforded by the JADES observations. We use the FRESCO grism data as well as the NIRSpec observations from PIDs 1210 and 1286 to measure spectroscopic redshifts for sources within our sample.

The GOODS-S and GOODS-N regions have been the target of deep HST observations, and we utilize existing HST/ Advanced Camera for Surveys (ACS) and WFC3 mosaics. We use the HST/ACS mosiacs from the Hubble Legacy Fields (HLF) v2.0 for GOODS-S and v2.5 for GOODS-N ($25' \times 25'$ for GOODS-S, and $20.'5 \times 20.'5$ for GOODS-N; Illingworth et al. 2013; Whitaker et al. 2019). We use data in the HST/ ACS F435W, F606W, F775W, F814W, and F850LP filters.

2.2. Data Reduction

2.2.1. JADES NIRCam

The data-reduction techniques used in this present study will be fully described in a future paper (S. Tacchella et al. 2024, in preparation), but they follow the methods outlined in Robertson et al. (2023) and Tacchella et al. (2023), which we briefly summarize here. For both the JADES GOODS-S and GOODS-N observations, the data were first reduced using the JWST calibration pipeline v1.9.2, with the JWST Calibration Reference Data System context map 1039. The raw images (`uncal` frames) are processed using the default JWST Stage 1 pipeline, which performs the detector-level corrections and results in count-rate images (`rate` frames).

The JWST pipeline Stage 2 involves flat-fielding and flux calibration, and was run largely with the default values. We convert from counts s^{-1} to MJy sr^{-1} following Boyer et al. (2022). During the data reduction, we discovered that the current long-wavelength (LW) flats used in the JWST pipeline result in nonastrophysical artifacts in the final mosaics. To mitigate this effect, we developed our own sky flats, stacking in each filter 80–200 source-masked raw `uncal` frames from across PIDs 1180, 1210, 1286, and JEMS. For F335M and F410M, where we did not have enough exposures to properly perform this stacking procedure, we instead constructed these sky flats via interpolation using the other wideband LW sky flats.

After Stage 2, we used custom corrections for common features seen in JWST/NIRCam data (Rigby et al. 2023). We fit and subtracted the $1/f$ noise (Schlawin et al. 2020) assuming a parametric model. To fit for the scattered-light "wisps" in the NIRCam short-wavelength channel, we constructed templates by stacking our images from the JADES program (PIDs 1180, 1210, 1286) as well as other publicly available programs (PIDs 1063, 1345, 1837, and 2738), and then subtracted these scaled templates for the short-wavelength channel detectors A3, A4, B3, and B4 (S. Tacchella et al. 2024, in preparation). The background was removed using the `photutils` Background2D class (Bradley et al. 2023).

We created our final mosaics using the JWST Pipeline Stage 3, after performing an astrometric alignment using a custom version of the JWST `TweakReg` software. In both GOODS-S and GOODS-N, we calculated the relative and absolute astrometric corrections for the individual images grouped by visit and by photometric band. We matched to sources in a reference catalog created from HST F814W and F160W mosaics with astrometry tied to Gaia Early Data Release 3 (Gaia Collaboration et al. 2021; G. Brammer, private communication). Following this alignment, we performed the default steps of Stage 3 of the JWST pipeline for each filter and visit. For our final mosaics we chose a pixel scale of $0.''03$ pixel^{-1} and drizzle parameter of `pixfrac=1` for both the short-wavelength and long-wavelength images.

2.2.2. FRESCO

The FRESCO (Oesch et al. 2023) NIRCam grism spectroscopic data in the F444W filter ($\lambda = 3.9$–$5.0\,\mu m$) were reduced and analyzed following the routines in Sun et al. (2023) and Helton et al. (2024). Here, we briefly summarize the main steps of the process. Because we aim to conduct a targeted emission-line search of [O III] and Hβ lines for our $z > 8$ galaxy candidates, and we do not expect any of them to have strong continuum emission that can be detected with grism data, we used a median-filtering technique to subtract out the remaining continuum or background on a row-by-row basis, following the methods outlined by Kashino et al. (2023). We extracted 2D grism spectra using the continuum-subtracted emission-line maps for all objects that are brighter than 28.5 AB mag in the F444W band and within the FRESCO survey area. The emission lines from sources fainter than 28.5 AB mag are not expected to be detected with FRESCO. The FRESCO short-wavelength parallel imaging observations were used for both astrometric and wavelength calibration of the F444W grism spectroscopic data.

We extracted 1D spectra from the 2D grism spectra using the optimal extraction algorithm (Horne 1986) utilizing the light profiles of sources in the F444W filter. We then performed automatic identifications of $>3\sigma$ peaks in 1D spectra (see Helton et al. 2024), and fit these detected peaks with Gaussian profiles. We tentatively assigned spectroscopic redshifts for $>3\sigma$ peaks, which minimizes the difference from the estimated photometric redshifts (Section 4.9). Visual inspection was performed on these tentative spectroscopic redshift solutions and spurious detections caused by either noise or contamination were removed. The final grism spectroscopic redshift sample of JADES sources will be presented in a forthcoming paper from the JADES collaboration.

2.2.3. JADES NIRSpec

In addition to FRESCO data, we discuss NIRSpec spectroscopic redshifts in Section 4.9, and these were reduced following the same procedure as outlined in Bunker et al. (2023a), Cameron et al. (2023), Curtis-Lake et al. (2023), and Bunker et al. (2023b). For the present study, we are only using the derived spectroscopic redshifts from these data.

2.3. Photometry

To compute the photometry from both the GOODS-S and GOODS-N mosaics in each filter, we used the software package `jades-pipeline` developed by authors B.R., B.D. J., and S.T. We began by creating an inverse-variance-weighted stack of the NIRCam F277W, F335M, F356W, F410M, and F444W images as an ultra-deep signal-to-noise ratio (S/N) image. From this S/N image, `jades-pipeline` utilizes software from the `Photutils` package to define a catalog of

Table 1
5σ Photometric Depth in JADES Areas Measured in $0\rlap{.}{''}2$ Apertures (Nanojansky)

Instrument	Filter	GOODS-S				GOODS-N	
		JADES Deep	JADES Medium	1210 Parallel	1286 Parallel	SE	NW
HST/ACS	F435W	2.33	10.77	10.9	10.43	7.75	9.40
HST/ACS	F606W	3.61	6.96	6.68	8.72	9.81	8.55
HST/ACS	F775W	2.22	15.79	16.46	15.03	13.61	9.21
HST/ACS	F814W	8.20	7.2	7.02	11.03	8.21	7.7
HST/ACS	F850LP	4.28	17.53	18.58	19.55	15.23	17.55
JWST/NIRCam	F070W	…	…	…	8.29	…	…
JWST/NIRCam	F090W	3.55	6.26	2.40	5.92	6.04	11.03
JWST/NIRCam	F115W	2.93	5.44	2.27	5.26	4.51	8.08
JWST/NIRCam	F150W	2.89	5.53	2.15	5.28	5.16	8.44
JWST/NIRCam	F182M	8.04	9.53	10.37	11.29	…	…
JWST/NIRCam	F200W	3.01	5.27	2.37	4.63	4.66	7.78
JWST/NIRCam	F210M	5.83	12.11	13.71	13.53	…	…
JWST/NIRCam	F277W	2.17	4.24	1.64	3.69	3.92	6.17
JWST/NIRCam	F335M	3.64	3.81	2.86	6.08	5.7	9.12
JWST/NIRCam	F356W	2.46	4.07	1.62	3.60	3.81	5.74
JWST/NIRCam	F410M	3.23	6.43	2.39	5.60	6.33	9.524
JWST/NIRCam	F430M	7.84	7.31	…	…	…	…
JWST/NIRCam	F444W	2.79	5.11	2.00	4.62	5.07	7.31
JWST/NIRCam	F460M	10.71	9.61	…	…	…	…
JWST/NIRCam	F480M	7.98	6.51	…	…	…	…

objects with five contiguous pixels above a S/N of 3 (Bradley et al. 2023), creating a segmentation map in the process.

From this catalog, we calculated circular and Kron aperture photometry on both the JWST NIRCam mosaics as well as the 30 mas pixel scale HLF mosaics (Illingworth et al. 2016; Whitaker et al. 2019) for ACS F435W, F606W, F775W, F814W, and F850LP filters. Forced photometry was performed using a range of aperture sizes. The uncertainties we report were measured by combining in quadrature both the Poisson noise from the source and the noise estimated from random apertures placed throughout the image (e.g., Labbé et al. 2005; Quadri et al. 2007; Whitaker et al. 2011). Elliptical Kron aperture fluxes were measured using Photutils with a Kron parameter of $K = 2.5$ and the default circularized radius 6 times larger than the Gaussian-equivalent elliptical sizes while masking segmentation regions of any neighboring source. We created empirical HST/ACS and JWST/NIRCam point-spread functions to estimate and apply aperture corrections assuming point source morphologies (Z. Chen 2023, private communication).

For this present study, we will fit to the JADES "CIRC1" ($0\rlap{.}{''}2$ diameter aperture) fluxes, which reduces the background noise associated with the use of larger apertures, and is appropriate given the typically small sizes found for high-redshift galaxies (Shibuya et al. 2015; Curtis-Lake et al. 2016; Robertson et al. 2023; Tacchella et al. 2023). We note that in Section 4.1 we discuss a sample of morphologically extended sources with photometric redshifts $z_a = 8-9$, although these sources consist of multiple smaller clumps, supporting the use of the smaller aperture photometry for their selection. We also use Kron aperture fluxes to calculate some derived parameters, such as the UV magnitude M_{UV} to better encompass the full flux from more extended sources. We estimated the 5σ limiting flux across both GOODS-S and GOODS-N from the $0\rlap{.}{''}2$ diameter fluxes and uncertainties. In Table 1, we report these 5σ limiting fluxes in nanojanskys for the following portions of GOODS-S: JADES Deep, JADES Medium, the 1210 Parallel, and the 1286 Parallel. In addition, we report the limiting fluxes

for both the shallower NW portion of the GOODS-N field and the SE portion. Understanding these depths is important for exploring the recovery of high-redshift galaxies across the JADES data.

3. Galaxy Selection at $z > 8$

Our final photometric catalogs span 20 optical and near-IR filters, including both HST/ACS and JWST/NIRCam observations. Because of the multiple data sets included in these catalogs, however, objects will only have coverage in a subset of these filters, with the maximum number being in the area of the JEMS survey in the GOODS-S region, where there is coverage in 19 filters (F070W was only observed in the 1286 parallel, no portion of which overlaps with JEMS). In this section, we describe how we identified $z > 8$ sources from the measured line-flux catalog. Throughout this study, we will identify sources using "JADES-GS-" or "JADES-GN-" followed by the R.A. and decl. values in decimal degrees corresponding to the source.

As discussed in the introduction (Section 1), we choose to employ template fitting in this study due to the large quantity of available data in the JADES data set, especially longward of the potential Lyα break for objects at $z > 8$. The rest-frame UV and optical continuum can be fit with the templates as well, better constraining the exact redshift than with color selection alone. In addition, potential strong optical emission lines such as [O III] $\lambda5007$ observed in high-redshift galaxies can boost the flux in photometric filters, and can be modeled with template fitting. The JADES data set includes multiple medium-band filters longward of 3 μm, where these effects can be more significant.

3.1. EAZY Photometric Redshifts

In order to estimate the redshifts of the GOODS-S galaxies, we used the photometric redshift code EAZY (Brammer et al. 2008). EAZY combines galaxy templates and performs a grid search as a function of redshift. We used the EAZY photometric redshift z_a, corresponding to the minimum χ^2 of the template
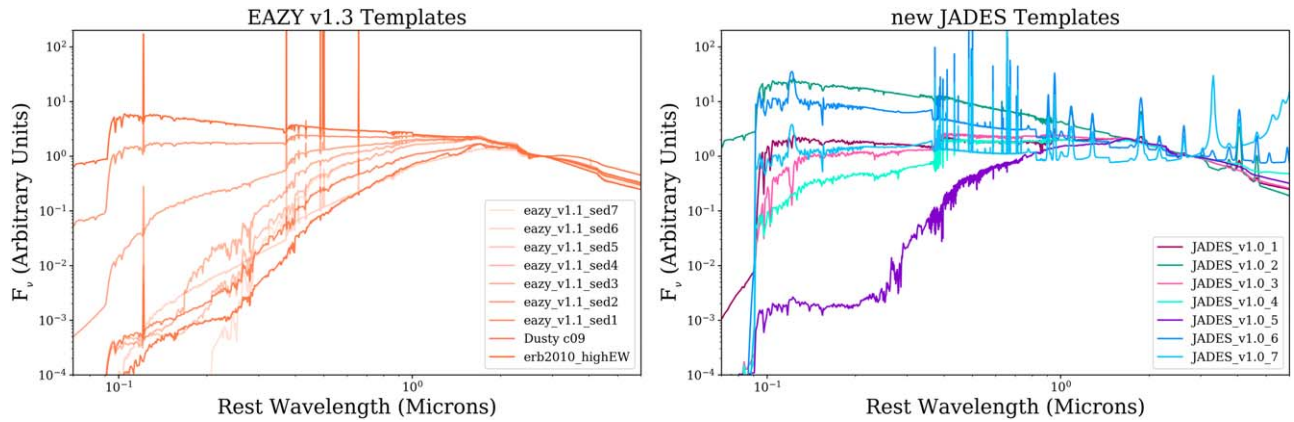
Figure 1. EAZY templates used in this work. In the left panel, we show the EAZY "v1.3" templates, and in the right panel, the new EAZY templates created for fitting to JADES galaxies. The templates are presented in F_ν units normalized at 2.8 μm. These templates include both UV-faint quiescent and UV-bright star-forming populations, and were both compiled from the literature and created using Flexible Stellar Population Synthesis (fsps; Conroy & Gunn 2010).

fits, to identify high-redshift galaxies. For the fits, we started with the EAZY "v1.3" templates, which we plot in the left panel in Figure 1. These templates include the original seven templates modified from Brammer et al. (2008) to include line emission, the dusty template "c09_del_8.6_z_0.019_chab_a-ge09.40_av2.0.dat," and the high-equivalent-width template taken from Erb et al. (2010; the equivalent width of [O III] λ5007 measured for the galaxy this template is derived from, Q2343-BX418, is 285 Å). We supplemented these with seven additional templates that were designed to optimize photometric redshift estimates for mock-galaxy observations from the JAGUAR simulations (Williams et al. 2018). These templates were created to better span the observed color space of the JAGUAR galaxies, including both red, dusty and blue, UV-bright populations. Similar to what has been demonstrated by other authors (e.g., Larson et al. 2023), we found that young galaxies with very high specific star formation rates can have very blue observed UV continuum slopes, which is made more complex due to strong nebular continuum and line emission (Topping et al. 2022). To aid in fitting these galaxies, we generated additional templates using Flexible Stellar Population Synthesis (fsps; Conroy & Gunn 2010), and added these to the "5 Myr" and "25 Myr" simple stellar population models introduced in Coe et al. (2006) for fitting blue galaxies in HUDF. We show our additional templates in the right panel of Figure 1, and we provide these templates online, hosted on Zenodo:10.5281/zenodo.7996500. Multiple templates from the full set contain nebular continuum and line emission, including that from Lyα.

In each redshift bin considered, EAZY combines all of the available templates together and applies an IGM absorption consistent with the redshift (Madau 1995). The best fit in that redshift bin, measured using the minimum χ^2, is recorded in a $\chi^2(z)$ surface that is output from the program. We explored the redshift range $z = 0.01-22$, with a redshift step size $\Delta z = 0.01$. We did not adopt any apparent magnitude priors, as the exact relationship between galaxy apparent magnitude and redshift at $z > 8$ is currently not well constrained, so any attempt to impose a prior would serve to only remove faint objects from the sample. To prevent bright fluxes from overly constraining the fits and to account for any photometric calibration uncertainties not captured by the offset procedure described below (e.g., due to detector specific offsets as observed in Bagley et al. 2023), we set an error floor on the photometry of

5%, and, additionally, we used the EAZY template error file "template error.v2.0.zfourge" to account for any uncertainties in the templates as a function of wavelength. We also explored the use of the EAZY templates discussed in Larson et al. (2023), which were used in finding high-redshift galaxies in the JWST Cosmic Evolution Early Release Science (CEERS) observations, and we describe how using these photometric redshifts affects our final sample in Section 4.8.

To match the EAZY template set to the observed fluxes in our catalog, we estimated photometric offsets with EAZY. We calculated the offsets for GOODS-S and GOODS-N data separately, where we first fit the observed photometry for a sample of galaxies with a S/N in F200W between 5 and 20, and calculated the offsets from the observed photometry to the template photometry. We then applied these offsets to the photometry and refit, iterating on this procedure. We list the final photometric offsets that we used for GOODS-S and GOODS-N, normalized to F200W, in Table 2. These offsets are within 10% of unity for all of the filters, with the exception of a large offset used for the F850LP observations in GOODS-N. We find that the F850LP depths are among the shallowest in our data set (Table 1), which is likely contributing to the large offset. While we observe differences between the GOODS-S and GOODS-N offsets, this is primarily driven by the comparison of the HST/ACS photometry to the NIRCam photometry. To demonstrate this, we recalculated the photometric redshifts but used identical filter sets between the sources in the two fields excluding the HST/ACS bands and the NIRCam medium bands F182M, F210M, F430M, F460M, and F480M, where we have limited coverage in these filters in GOODS-S and GOODS-N. The median difference in the photometric offsets between the GOODS-S and GOODS-N fits for the remaining filters as provided in Table 2 is 0.006, with a standard deviation of 0.012. However, when we calculate the offsets without the HST/ACS bands or the NIRCam medium bands, the median difference goes down to 0.001 and a standard deviation of only 0.004, consistent with no difference.

We used the $\chi^2(z)$ values output from EAZY to calculate a probability $P(z)$ assuming a uniform redshift prior: $P(z) = \exp[-\chi^2(z)/2]$, where we normalize such that $\int P(z) \, dz = 1.0$. The $P(z)$ and $\chi^2(z)$ values allowed us to calculate $P(z > 7)$, the summed probability from EAZY that the galaxy is at $z > 7$, as well as the χ^2 minimum for EAZY fits restricted to

Table 2
EAZY-derived Photometric Offsets, Normalized to F200W

Instrument	Filter	GOODS-S Offset	GOODS-N Offset
HST	F435W	1.021	1.072
HST	F606W	1.002	0.976
HST	F775W	1.009	0.996
HST	F814W	0.962	0.998
HST	F850LP	0.919	0.774
NIRCam	F070W	0.981	...
NIRCam	F090W	0.987	1.012
NIRCam	F115W	1.008	1.020
NIRCam	F150W	0.994	0.989
NIRCam	F182M	1.001	0.991
NIRCam	F200W	1.000	1.000
NIRCam	F210M	1.014	1.006
NIRCam	F277W	0.998	0.990
NIRCam	F335M	1.035	1.024
NIRCam	F356W	1.057	1.047
NIRCam	F410M	1.071	1.057
NIRCam	F430M	1.014	...
NIRCam	F444W	1.015	1.009
NIRCam	F460M	0.956	...
NIRCam	F480M	1.017	...

$z < 7$. These statistics, and others, are helpful for identifying and removing interlopers from our sample.

In Figure 2, we show the EAZY fit to an object in GOODS-S, JADES-GS-53.17551-27.78064, along with the $P(z)$ surface, and the JADES NIRCam thumbnails. The source is an F115W dropout, with no visible flux at shorter wavelengths. The fit constrained at $z < 7$ produces significantly more F115W flux than is observed, lending evidence of this galaxy being at $z > 9$.

3.2. High-redshift Galaxy Selection and Catalogs

Because of the extensive deep photometric data for the GOODS-S and GOODS-N fields, we chose to use the EAZY photometric redshifts for finding $z > 8$ candidates, as template fitting utilizes more photometric data points in the fit than color selection by itself. Following work done in the literature (Finkelstein et al. 2023), we selected galaxies at $z > 8$ by imposing these rules on the EAZY fits:

1. The redshift of the fit corresponding to the minimum χ^2, z_a, must be greater than 8.
2. The S/N in at least two photometric bands must be above 5. For this study, we chose NIRCam F115W, F150W, F200W, F277W, F335M, F356W, F410M, or F444W, as these filters are longward of the Lyα break at $z > 8$. We used the photometry derived using $0\overset{''}{.}2$ diameter apertures for measuring this S/N.
3. The summed probability of the galaxy being above $z > 7$ must be greater than 70%, or $\int_7^{22} P(z)dz > 0.7$.
4. The difference between the overall minimum χ^2 and the minimum χ^2 at $z < 7$, $\Delta\chi^2$, must be greater than 4.
5. There should be no object within $0\overset{''}{.}3$ (10 pixels in the final JADES mosaics), or within the object's bounding box, that is 10 times brighter that the object.

For this study, we targeted galaxies at $z_a > 8$ as galaxies above this redshift should have no observed flux in the JWST/NIRCam F090W filter. This allows us to use the deep JADES
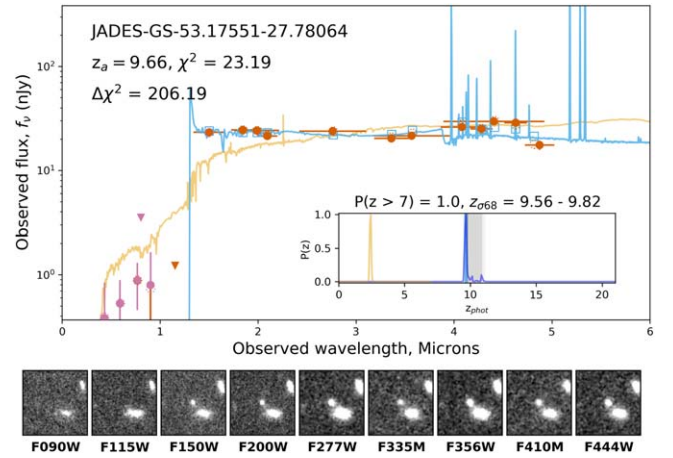

Figure 2. Example best-fit SED for object JADES-GS-53.17551-27.78064, at the best-fit redshift $z_a = 9.66$. We plot the NIRCam photometry with red points, and the HST photometry with light purple points. The error bars represent the 1σ uncertainties on the fluxes. We plot 2σ upper limits with downward-pointing triangles. The blue line represents the fit corresponding to z_a and the gold line shows the best fit at $z < 7$. We show the minimum χ^2 value for the z_a fit, as well as the $\Delta\chi^2$ value corresponding to the difference between the minimum χ^2 and the χ^2 for the fit at $z < 7$. In the inset, we plot $P(z)$, with the 1σ, 2σ, and 3σ uncertainty regions derived from the $P(z)$ surface with shades of gray, and z_a with a blue line, along with the $P(z)$ distribution for the $z < 7$ best fit in gold (also normalized to 1). Above the inset we provide the summed probability of the source being at $z > 7$, along with the EAZY redshifts corresponding to $\sigma_{68,low}$ and $\sigma_{68,high}$. Below the SED we plot $2'' \times 2''$ thumbnails for the JADES NIRCam filters.

F090W observations to aid in visually rejecting lower-redshift contaminants. The second requirement, that the source be detected in multiple bands, was chosen to ensure that the sources we selected were not artifacts found in individual exposures such as cosmic rays or bad pixels. We imposed the EAZY $\int_7^{22} P(z) > 0.7$ (which we will shorten to "$P(z > 7)$") and $\Delta\chi^2$ limits in order to help remove objects where EAZY could fit the observed SED at low redshift with high probability. In Harikane et al. (2023), the authors recommend the use of a more strict cut, $\Delta\chi^2 > 9$, and we consider this cut in Section 5. We also, in Section 4.4, discuss those objects where $\Delta\chi^2 < 4$ in our sample, as these sources, though faint, may contain true high-redshift galaxies that should be considered. Finally, we remove objects with close proximity to bright sources because of the possibility of selecting tidal features or stellar clusters near to the edges of relatively nearby galaxies. We list those objects that satisfied our other requirements but were close to a brighter source, along with discussion of these targets, in Section 4.5. We chose not to implement a direct cut on χ^2 as this metric is dependent on the flux uncertainties, which vary across the field in such a way as to make a comparison of the value between objects difficult and potentially nonmeaningful. We still report the resulting χ^2 values, however. In comparison, the $\Delta\chi^2$ value is calculated from two fits to the same photometry and uncertainties, and is helpful in exploring the relative goodness of fits at different redshifts.

These cuts resulted in 1078 objects in GOODS-S and 636 objects in GOODS-N. From here, we began the process of visual inspection, first to remove obvious nonastrophysical data artifacts, including extended diffraction spikes from stars, and hot pixels caused by cosmic rays. We also removed extended, resolved, low-redshift dusty sources, many of which were not

Table 3
Overview of Columns in the $z > 8$ Source Catalog

Column	Description
1	JADES ID
2, 3	R.A. and decl., in decimal degrees, of the source
4	$m_{F277W, \, Kron}$ (AB)
5–11	EAZY z_a, $\sigma_{68,low}$, $\sigma_{68,high}$, $\sigma_{95,low}$, $\sigma_{95,high}$, $\sigma_{99,low}$, $\sigma_{99,high}$
12	EAZY $\int_{7}^{22} P(z)dz$
13	EAZY minimum χ^2
14	EAZY minimum z_a ($z < 7$)
15	EAZY χ^2 ($z < 7$)
16	EAZY $\Delta\chi^2$
17, 18	Spectroscopic redshift, source (FRESCO or NIRSpec)
19	M_{UV}
20	Flag indicating the source is fit by a brown-dwarf model within $\Delta\chi^2 < 4$
21	Flag indicating whether or not the source is unresolved ($r_{eff,F444W} < 0.''063$)
22, 23	HST/ACS F435W flux, 1σ uncertainty (nJy)
24, 25	HST/ACS F606W flux, 1σ uncertainty (nJy)
26, 27	HST/ACS F775W flux, 1σ uncertainty (nJy)
28, 29	HST/ACS F814W flux, 1σ uncertainty (nJy)
30, 31	HST/ACS F850LP flux, 1σ uncertainty (nJy)
32, 33	JWST/NIRCam F070W flux, 1σ uncertainty (nJy)
34, 35	JWST/NIRCam F090W flux, 1σ uncertainty (nJy)
36, 37	JWST/NIRCam F115W flux, 1σ uncertainty (nJy)
38, 39	JWST/NIRCam F150W flux, 1σ uncertainty (nJy)
40, 41	JWST/NIRCam F182M flux, 1σ uncertainty (nJy)
42, 43	JWST/NIRCam F200W flux, 1σ uncertainty (nJy)
44, 45	JWST/NIRCam F210M flux, 1σ uncertainty (nJy)
46, 47	JWST/NIRCam F277M flux, 1σ uncertainty (nJy)
48, 49	JWST/NIRCam F335M flux, 1σ uncertainty (nJy)
50, 51	JWST/NIRCam F356W flux, 1σ uncertainty (nJy)
52, 53	JWST/NIRCam F410M flux, 1σ uncertainty (nJy)
54, 55	JWST/NIRCam F430M flux, 1σ uncertainty (nJy)
56, 57	JWST/NIRCam F444W flux, 1σ uncertainty (nJy)
58, 59	JWST/NIRCam F460M flux, 1σ uncertainty (nJy)
60, 61	JWST/NIRCam F480M flux, 1σ uncertainty (nJy)
62	JADES footprint region

Note. We provide these values for the primary $z > 8$ sample with $\Delta\chi^2 > 4$, as well as the subsamples outlined in the text: $\Delta\chi^2 < 4$ and those proximate to brighter sources.

visible in HST imaging. These sources were identified by very red slopes between 1 and 5 μm, and have half-light radii $r_{half} \gtrsim 1''$ in the filters where they are observed. These sources comprise only ∼0.4% of the objects that satisfy our cuts. After removing these sources, we were left with 580 possible objects in GOODS-S and 212 objects in GOODS-N. There is a much larger fraction of spurious sources in GOODS-N as compared to GOODS-S as these data had a larger number of bright pixels and cosmic rays, which primarily affected the NIRCam LW channels.

After this initial inspection, authors K.H., J.H., D.E., M.W. T., C.N.W., L.W., and C.S. independently graded each target with a grade of "Accept," "Reject," or "Review." For those objects where 50% or more of the reviewers accepted the candidate, it was then added to the final candidate list. In cases where greater than 50% of the reviewers chose to reject the candidate, this candidate was removed entirely from the candidate list. In all other cases (57 objects in GOODS-N and 102 objects in GOODS-S), the reviewers did one more round of visual inspection with only the grades Accept or Reject, with a larger discussion occurring for objects where necessary. Again, a 50% of Accept grades was required for

these galaxies under review to be listed as part of the final sample.

4. Results

Our final $z > 8$ samples consist of 535 objects in GOODS-S and 182 objects in GOODS-N. In Table 3, we provide descriptions of the columns in our final catalog; the catalog itself is provided as an online table on Zenodo doi:10.5281/zenodo.7996500. We include $0.''2$ diameter aperture photometry in each of the observed photometric bands, as well as the EAZY z_a, χ^2, $P(z > 7)$, and $\Delta\chi^2$ values used in selecting the galaxies. We also provide the σ_{68}, σ_{95}, and σ_{99} confidence intervals estimated from the $P(z)$ distribution. In this table, we also list the $z > 8$ candidates that have EAZY $\Delta\chi^2 < 4$, and we will discuss these sources in Section 4.4. Similarly, in our output table, we list those $z > 8$ candidates that were either within $0.''3$ or within the bounding box of a target 10 times brighter than the candidate, which we discuss in Section 4.5.

We show the positions of the GOODS-N sources in the left panel and the GOODS-S sources in the right panel of Figure 3. In these figures, we include both those with EAZY $\Delta\chi^2 > 4$ (dark points) and EAZY $\Delta\chi^2 < 4$ (lighter points). The relatively
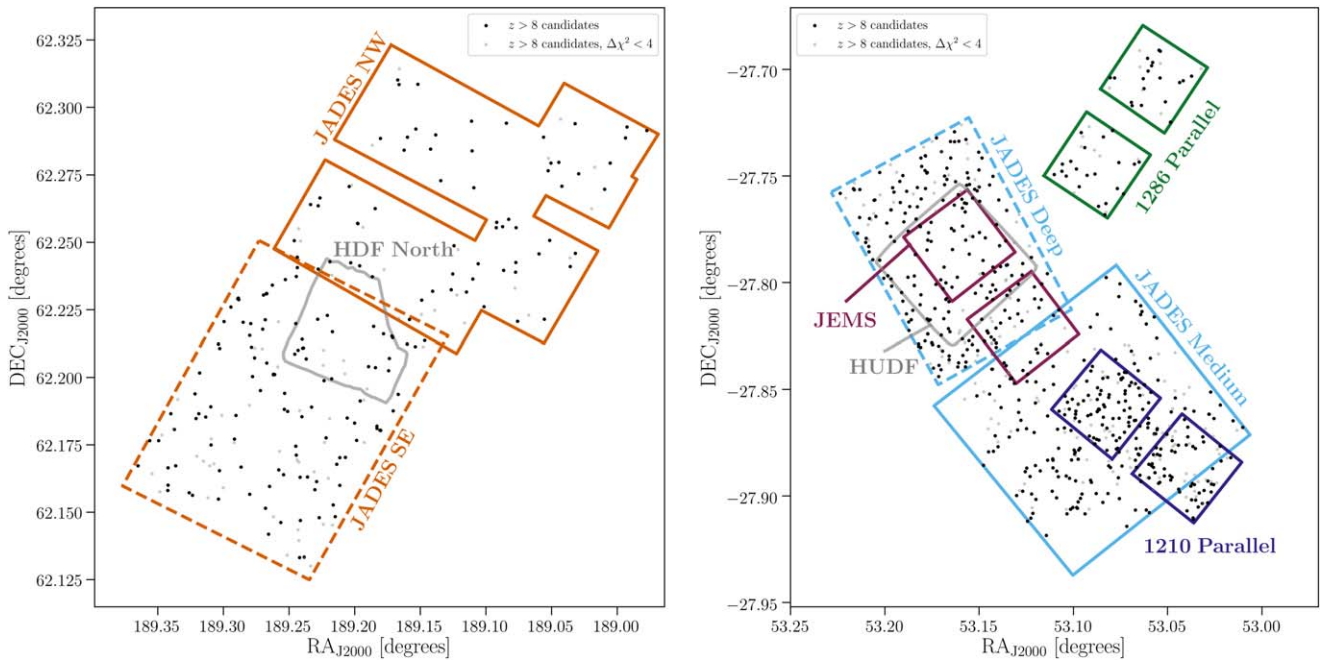
Figure 3. Left: GOODS-N footprint showing the positions of the $z > 8$ candidates. The southeastern portion (dashed) of the GOODS-N area is deeper than the northwestern portion (solid), resulting in a larger density of candidate high-redshift galaxies. In gray, we plot the outline of the Hubble Deep Field (North) (Williams et al. 1996) as a comparison to the JADES survey area. Right: GOODS-S footprint. The dashed blue outline highlights the JADES Deep GOODS-S area, and the solid blue outline highlights the JADES Medium GOODS-S region. The colored squares denote additional NIRCam pointings from the JEMS survey (burgundy), the 1210 parallels (purple), and the 1286 parallels (green). In gray, we plot the outline of the Hubble UDF (Beckwith et al. 2006). There is a noticeable increase in the density of sources in the JADES Deep and the ultra-deep 1210 parallel footprint.

higher density of sources in the southern portion of the GOODS-N observations compared to the northern portion is a result of the increased observational depth in that region. In GOODS-N, we find 2.1 objects in our $z > 8$ sample per square arcmin in the northeast (NE) footprint, and 4.3 objects per square arcmin in the SW footprint. Similarly, the deepest portions of the JADES GOODS-S coverage are the large rectangular JADES Deep region, and the smaller 1210 parallels, where a significantly higher density of objects are detected. In GOODS-S, we find 7.8 objects in our $z > 8$ sample per square arcmin in JADES Deep, 4.5 objects per square arcmin in JADES Medium, 4.1 objects per square arcmin in the 1286 parallel, and 13.9 objects per square arcmin in the 1210 parallel.

In Figure 4, following similar work done in the literature (Austin et al. 2023; Finkelstein et al. 2023; Pérez-González et al. 2023), we show the F277W observed AB magnitude measured using a Kron aperture against the EAZY photometric redshift for each candidate $z > 8$ galaxy in GOODS-S and GOODS-N. Across the top we show the distribution of the photometric redshifts, and on the right side we show the F277W magnitude distribution for the photometric redshift sample as well as the GOODS-N and GOODS-S sample independently. For those objects where we have spectroscopic redshifts from either NIRSpec or FRESCO, we plot this value instead of the photometric redshift, and indicate those galaxies with larger points with black outlines. The GOODS-S sample, by virtue of the deeper coverage, extends to much fainter F277W magnitudes. On this diagram, the galaxy GN-z11 (Oesch et al. 2016; Bunker et al. 2023a; Tacchella et al. 2023) is the brightest source, as one of two galaxies at $m_{F277W,Kron} < 26$ (the other is JADES-GS-53.10394-27.89058, at $z_a = 8.35$). The redshifts seen in the main

panel are discrete because of how EAZY fits galaxies at specific redshift steps.

In Figure 4, we can see how the usage of wide filters for estimating photometric redshift leads to relative dearths of objects at $z \sim 10$ and $z \sim 13$, as these redshifts are where the Lyα break is between the F090W, F115W, and F150W filters. This is an artificial effect—for Lyα-break galaxies, estimations of precise redshifts are highly predicated on the flux in the band that probes the break, and when the break sits between filters, the resulting redshifts are more uncertain. For example, faint galaxies at $z \sim 9-11$ can have similar SEDs where there is flux measured in the F150W filter and none measured in the F115W filter. This degeneracy results in photometric redshifts of these galaxies of $z_a \sim 9.5$, with broad χ^2 minima reflecting larger redshift uncertainties. At slightly higher redshifts, however, the Lyα break moves into the F150W filter and this results in red F150W − F200W colors, leading to more precise photometric redshifts. This same effect is seen between the F150W and F200W filters at $z \sim 13$. The usage of medium-band filters, like NIRCam F140M, F162M, F182M, and F210M, would help mitigate this effect somewhat for galaxies at these redshifts. We further explore these gaps by simulating galaxies across a uniform redshift range in Appendix A.

In this section, we discuss the candidates in three subcategories: $z_a = 8-10$ (Section 4.1), $z_a = 10-12$ (Section 4.2), and $z_a > 12$ (Section 4.3). For each subcategory we describe the properties of the sample, plot example SEDs for galaxies spanning the magnitude and redshift range, and discuss notable examples.

4.1. $z_{phot} = 8-10$ Candidates

We find 547 total galaxies and galaxy candidates combined across the JADES GOODS-S (420 sources) and GOODS-N
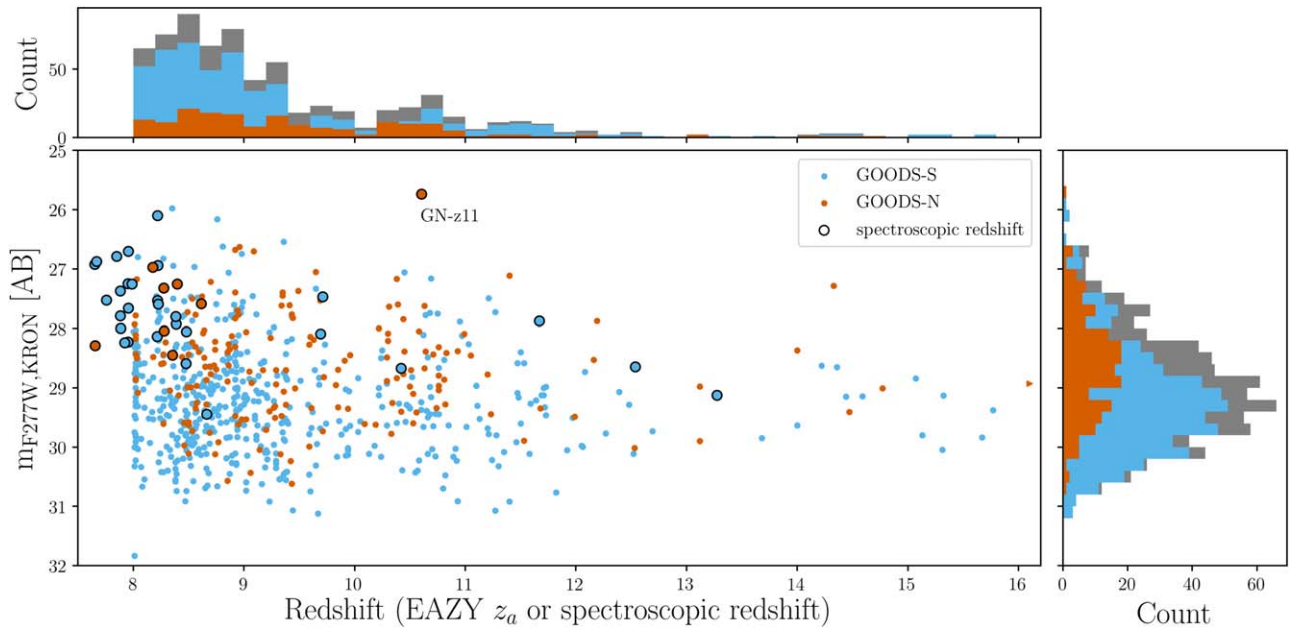
Figure 4. F277W AB Kron magnitude plotted against the best-fitting EAZY z_a photometric redshift for the 717 galaxies and candidate galaxies in the GOODS-S (blue) and GOODS-N (red) $z > 8$ samples. Along the top we show the redshift distribution for the full sample (gray) as well as the GOODS-S and GOODS-N samples. On the right we show the magnitude distribution in a similar manner. The points colored with dark circles are plotted with the available spectroscopic redshifts for those sources, which, in many cases, extends to $z < 8$. We discuss these sources in Figure 4.9. There is a lack of sources at $z \sim 10$ because of how the Lyα break falls between the NIRCam F115W and F150W at this redshift, making exact photometric redshift estimates difficult. The brightest source in the sample is the spectroscopically confirmed galaxy GN-z11 at $z_{spec} = 10.6$, and the highest-redshift spectroscopically confirmed source is JADES-GS-z13-0 at $z_{spec} = 13.2$. There is one source, JADES-GN-189.15981+62.28898, at $z_a = 18.79$, which we plot as a right-facing arrow in the plot and discuss in Section 4.3.

(127 sources) areas at $z_a = 8-10$. We show a subsample of the EAZY SED fits and the JADES thumbnails for eight example candidate high-redshift galaxies in this photometric redshift range in Figure 5. In each plot, we show both the minimum χ^2 fit, as well as the fit constrained to be at $z < 7$. We chose these objects from the full sample to span a range of F277W Kron magnitudes as well as photometric redshifts.

Because of the availability of both NIRSpec and FRESCO spectroscopy for our sample, there are 34 (27 in GOODS-S and seven in GOODS-N) galaxies in this photometric redshift range where a spectroscopic redshift has been measured. For 14 of these sources (13 in GOODS-S and one in GOODS-N), the resulting spectroscopic redshift $z_{spec} = 7.65-8.0$. Because these objects satisfied our photometric redshift selection criteria, we choose to include them in our sample, and discuss their spectroscopic redshifts in Section 4.9.

There are a number of sources in this photometric redshift range with extended morphologies, often seen in the JADES data as multiple clumps observed in the images at shorter wavelengths. In Figure 6, we show a subsample of nine resolved galaxies with $z_a = 8-9$. For each object we show the F090W, F115W, and F356W thumbnails, along with a color image combining these three filters. Each thumbnail is $2''$ on a side, showcasing the resolved sizes of some of these targets. At $z = 8-10$, $1''$ corresponds to 4.6–4.9 kpc, and we provide a scale bar of $0.''5$ in each panel. At these redshifts, F090W is to the blue of the Lyα break, so the galaxies should not appear in this filter, F200W spans the rest-frame UV, and F356W spans the rest-frame optical continuum. We are then seeing UV-bright star-forming clumps in the F200W filter, and rest-frame $\sim$4000 Å stellar continuum in F356W. We show two sources, JADES-GS-53.1571-27.83708 (top row, left column) and JADES-GS-53.08738-27.86033 (top row, middle column), which have spectroscopic redshifts from FRESCO at $z_{spec} =$

7.67 and $z_{spec} = 7.96$, respectively, as indicated below the photometric redshifts in the color panel.

These nine sources show multiple irregular morphologies, and many are elongated. JADES-GN-189.18051+62.18047 is an especially complex system at $z_a = 8.92$ with four or five clumps that span almost 7 kpc at this photometric redshift, similar to the "chain of five" F150W dropout system presented in Yan et al. (2023). Five of the extended sources we highlight were previously presented in the literature: JADES-GS-53.1571-27.83708, JADES-GS-53.08738-27.86033, JADES-GS-53.08174-27.89883, JADES-GS-53.1459-27.82279, and JADES-GS-53.10393-27.89059 (McLure et al. 2013; Bouwens et al. 2015; Finkelstein et al. 2015; Harikane et al. 2016; Bouwens et al. 2021). Given the depth and resolution of NIRCam, we can see new details for these sources from what was observed in the HST ACS and WFC3 observations, such as the nearly $\sim$0.''8-long haze to the NE for JADES-GS-53.10393-27.89059, which corresponds to about 4 kpc at the candidate photometric redshift.

4.2. $z_{phot} = 10-12$ Candidates

We find a total of 137 galaxies and candidate galaxies at at $z_{phot} = 10-12$: 92 in GOODS-S and 45 in GOODS-N. We show the EAZY SED fits and the JADES thumbnails for eight example candidates in this photometric redshift range in Figure 7.

In the GOODS-S region, this redshift range includes two of the spectroscopically confirmed galaxies from Robertson et al. (2023) and Curtis-Lake et al. (2023), JADES-GS-z10-0 ($z_{spec} = 10.38^{+0.07}_{-0.06}$) and JADES-GS-z11-0 ($z_{spec} = 11.58^{+0.05}_{-0.05}$). The EAZY photometric redshifts for these targets are $z_a = 10.84$ for JADES-GS-z10-0 and $z_a = 12.31$ for JADES-GS-z11-0. Both photometric redshifts are higher than the measured spectroscopic
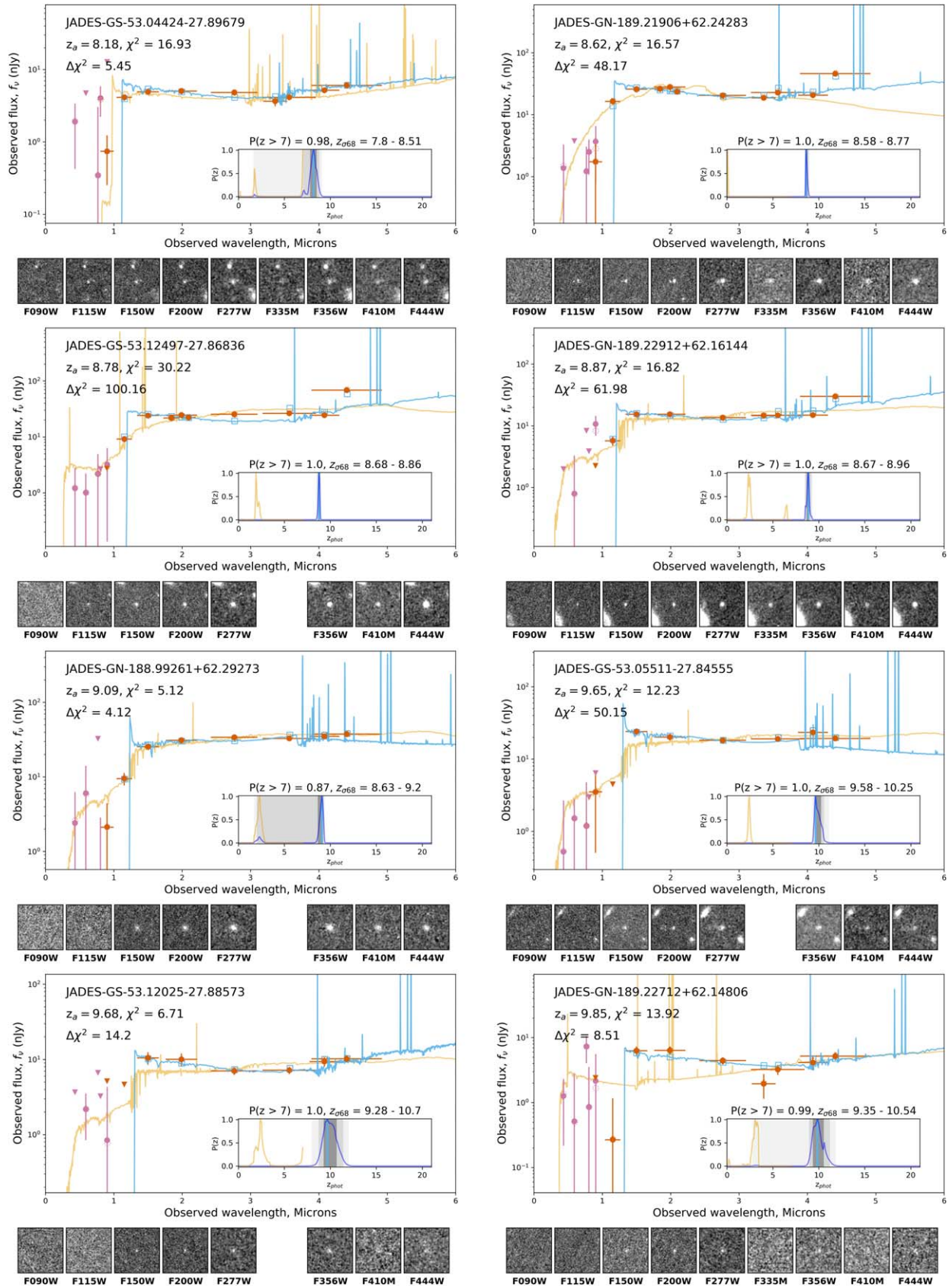
Example $z = 8 - 10$ Candidates

Figure 5. Example SEDs for eight $\Delta\chi^2 > 4$ candidate GOODS-S and GOODS-N galaxies at $z_a = 8-10$. In each panel, the colors, lines, and symbols are as in Figure 2.
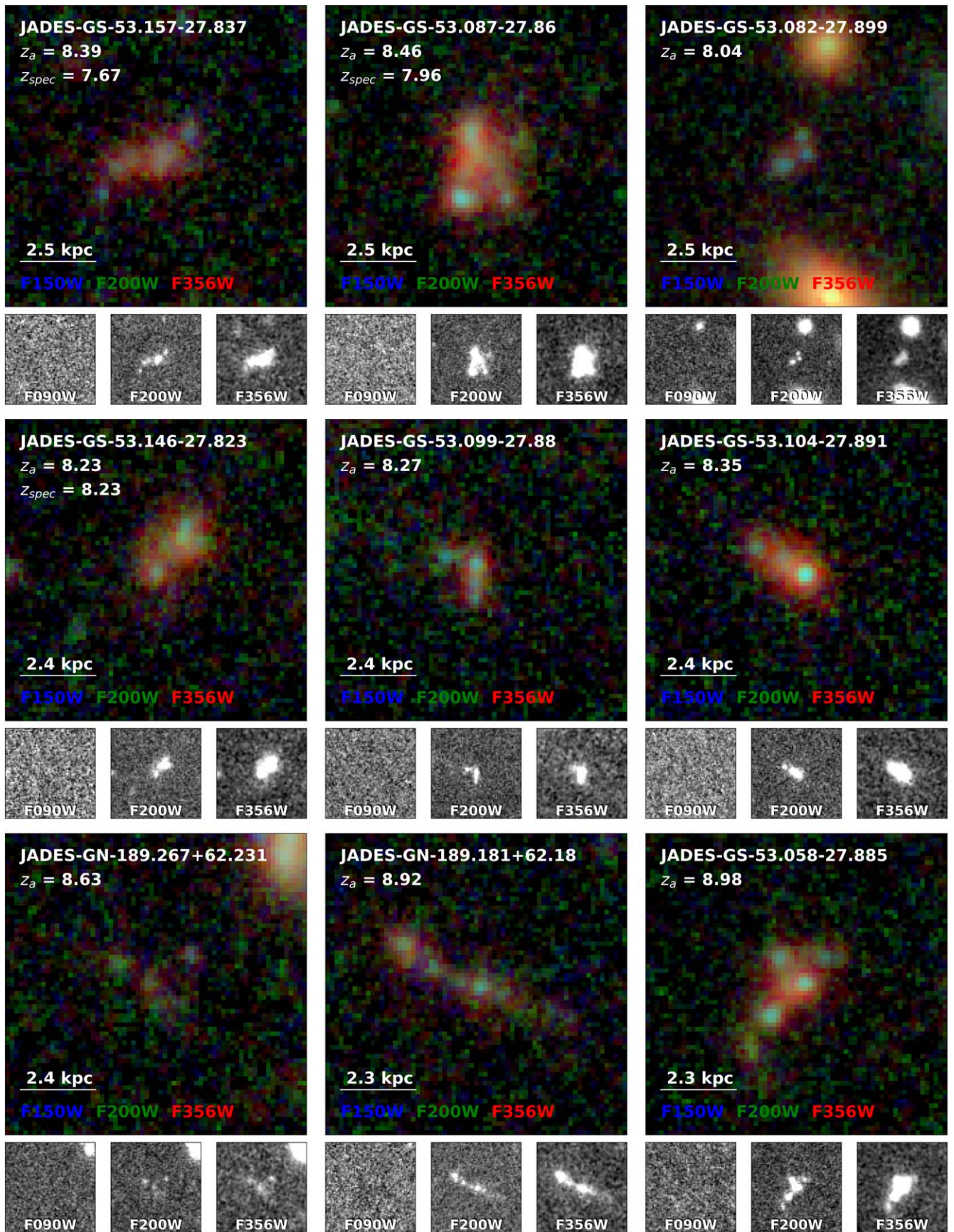
Figure 6. Color thumbnails for a selection of nine $z_a = 8-9$ resolved galaxies with multiple components. Each thumbnail is $2''$ on a side, and we include a size bar showing $0\rlap{.}{''}5$ for each object. The color image is composed of F356W, F200W, and F090W as red, green, and blue, respectively. We also show images in those filters for each object separately to demonstrate the dropout nature of these objects in the F090W filter.

Example $z = 10 - 12$ Candidates
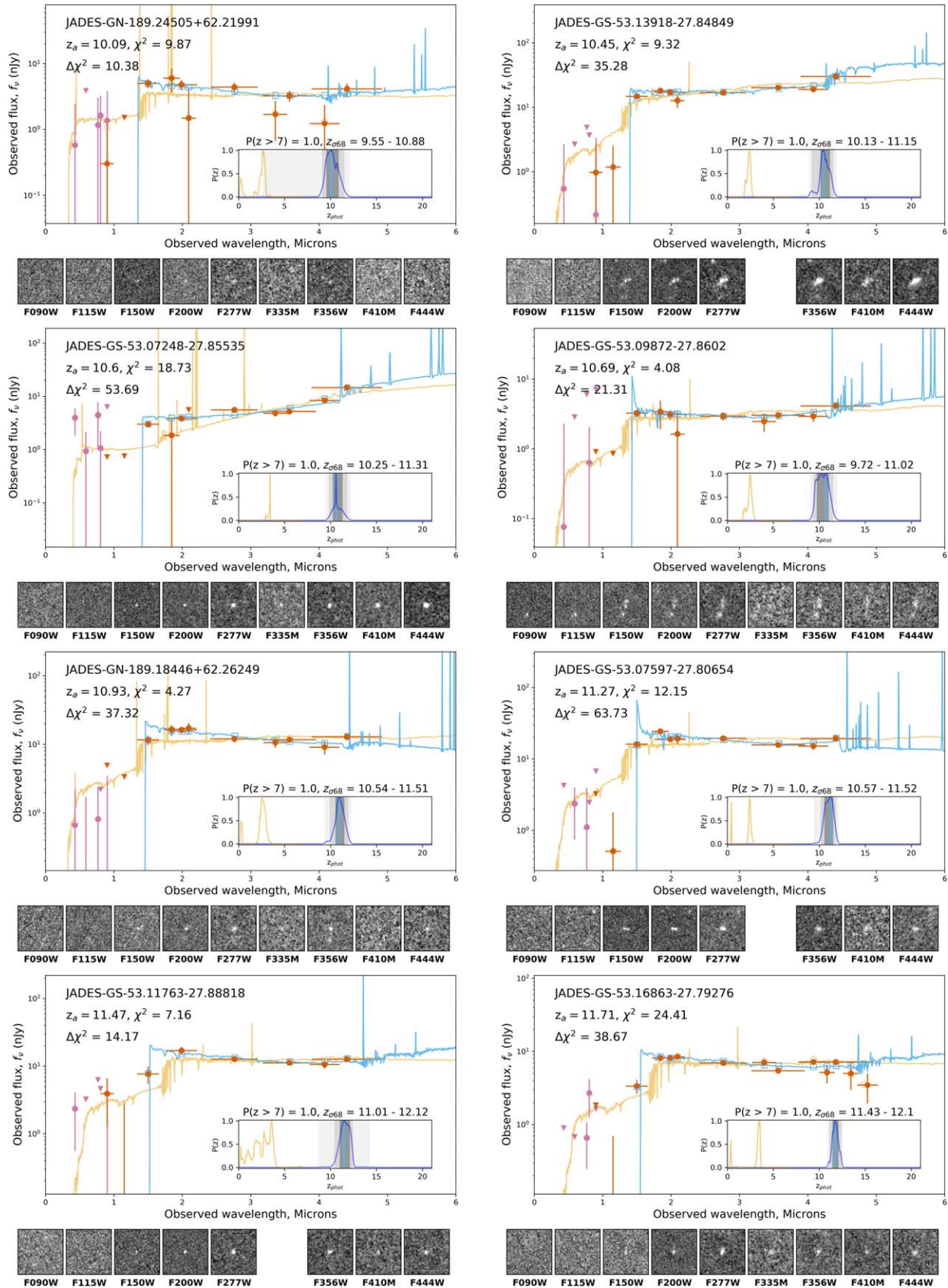
Figure 7. Example SEDs for eight $\Delta\chi^2 > 4$ candidate GOODS-S and GOODS-N galaxies at $z_a = 10-12$. In each panel, the colors, lines, and symbols are as in Figure 2.

redshift, but considering the $P(z)$ uncertainty in both measurements, the measurements are within 2σ of the true values. Indeed, the $\Delta\chi^2$ between the minimum value corresponding to z_a and the value at $z_{\rm spec}$ is 10.25 for JADES-GS-z10-0 and 1.75 for JADES-GS-z11-0. In Robertson et al. (2023), the authors estimate photometric redshifts for these sources using the Bayesian stellar population synthesis fitting code Prospector (Johnson et al. 2021) and recover $P(z)$ surfaces that are similarly offset to higher values than the spectroscopic redshifts. In the GOODS-N region, we find the brightest object overall in our sample (a Kron F277W aperture magnitude of 25.73 AB), GN-z11, discussed at length in Tacchella et al. (2023) and spectroscopically confirmed to lie at $z = 10.603 \pm 0.001$ in Bunker et al. (2023a). In our EAZY fit, we estimate $z_a = 11.0$, which is within 2σ of the spectroscopic redshift but, again, higher than the spectroscopic redshift. We further explore this difference in Section 4.9.

In Tacchella et al. (2023), the authors identify nine galaxies within 10 comoving Mpc ($212''$) of GN-z11 that have photometric redshifts between $z_a = 10$ and 11. Six of these sources are included in our $\Delta\chi^2 > 4$ sample (JADES-GN+189.1162 +62.22007, JADES-GN+189.07603+62.2207, JADES-GN +189.12549+62.2382, JADES-GN+189.08667+62.2395, JADES-GN+189.05971+62.2457, and JADES-GN+189. 05166+62.2507, given as 465, 544, 4418, 4811, 6862, and 8597 in Tacchella et al. 2023), while the other three sources (JADES-GN-189.07355+62.2375, JADES-GN-189.19975 +62.2703, and JADES-GN-189.05413+62.2179, given as 4155, 13543, and 62240 in Tacchella et al. 2023) are not in our final sample as these sources did not satisfy the requirement of having a flux S/N > 5 in at least two bands to the red of the potential Lyα break, or in the case of JADES-GN-189.07355 +62.2375, this source has $z_a < 8$ with the updated photometry in this study.

We want to highlight three galaxies seen in Figure 7 because of their extended, somewhat complex morphologies. JADES-GS-53.13918-27.84849 ($z_a = 10.45$, first row, right column), an F115W dropout, has three components and spans $0''5$, which is 2 kpc at this photometric redshift. We observe an increase in the F444W flux over what is seen at 3–4 μm, which could either be a result of [O II]λ3727 emission at this redshift or evidence of a Balmer break. The F115W dropout JADES-GS-53.09872-27.8602 ($z_a = 10.69$, second row, right column) is the southern clump of two morphologically distinct components separated by $0''3$ (1.2 kpc at this photometric redshift) in the rest-frame UV, which becomes less distinct at longer wavelengths. The northern clump, JADES-GS-53.09871-27.86016 ($z_a = 9.59$), is also in our sample, but the EAZY fit prefers a lower photometric redshift which is consistent to within 1σ. Finally, JADES-GS-53.07597-27.80654 ($z_a = 11.27$, third row, right column) consists of two bright, connected clumps separated by $0''2$ (580 pc at this photometric redshift). The sources are detected as separate clumps in the relatively shallower FRESCO F182M and F210M data as well. These sources could be interacting seed galaxies or star-forming clumps in the very early Universe.

4.3. $z_{phot} > 12$ Candidates

We find 33 galaxies and candidate galaxies across both the JADES GOODS-S (23 sources) and GOODS-N (10 sources) footprints at $z > 12$. We show their SEDs and thumbnails for eight examples in Figure 8, and we show the remaining in Figures 18, 19, and 20 in Appendix B. For objects at these redshifts, the Lyα break falls in the F150W filter at $z = 12$, in

between the F150W and F200W filters at $z = 13.2$, and in between the F200W and F277W filters at $z = 17.7$. The objects in our $z > 12$ sample, then, are a mixture of solid F150W dropouts and more tentative galaxies that show evidence for faint F200W flux associated with the Lyα break lying in that filter.

Our sample in this redshift range includes the other two high-redshift spectroscopically confirmed galaxies from Robertson et al. (2023) and Curtis-Lake et al. (2023), JADES-GS-z12-0 ($z_{\rm spec} = 12.63^{+0.24}_{-0.08}$) and JADES-GS-z13-0 ($z_{\rm spec} = 13.20^{+0.04}_{-0.07}$). We estimate EAZY photometric redshifts for these targets of $z_a = 12.46$ for JADES-GS-z12-0 and $z_a = 13.41$ for JADES-GS-z13-0. While both photometric redshifts are quite uncertain due to the width of the bands used to probe the Lyα break, the range of uncertainties based on the EAZY σ_{68} redshifts are consistent with the spectroscopic redshifts.

Because of the importance of these galaxies toward understanding galaxy formation in the very early Universe, we will discuss the candidate galaxies in this redshift range individually, in order of decreasing photometric redshift. In our descriptions, we include brief discussions of two of the spectroscopically confirmed galaxies from Robertson et al. (2023) and Curtis-Lake et al. (2023), JADES-GS-z12-0, and JADES-GS-z13-0, but we refer the reader to these papers for more detailed discussions of these sources.

JADES-GN-189.15981+62.28898 ($z_a = 18.79$). This F200W dropout, the highest-redshift candidate in our sample, is clearly detected in multiple LW filters. There is no detection in the F200W filter, and we calculate a dropout color assuming a 2σ upper limit on the F200W flux of $m_{\rm F200W} - m_{\rm F277W} > 1.29$. While this source lies in the relatively shallower GOODS-N NW portion of the survey, the large $\Delta\chi^2$ provides strong evidence for this source being at high redshift.

JADES-GS-53.12692-27.79102 ($z_a = 15.77$). This is one of the more intriguing objects in our sample, as it is a relatively bright ($m_{\rm F277W,Kron} = 29.37$) F150W dropout detected at greater than 16σ in all of the detection bands. While there may be F115W flux observed in the thumbnail, it is only at S/N = 1.76. Caution should be exercised in adopting the derived redshift for this source as a result, since this object's fluxes are consistent with it being at $z = 5$.

JADES-GS-53.0541-27.70399 ($z_a = 15.67$). This F150W dropout has quite large photometric redshift uncertainties, but the σ_{68} range is still consistent with it being at $z > 12$. The source $1''$ to the east is a potential F090W dropout with $z_a = 8.24$, but we measure $P(z < 7) = 0.68$ from the EAZY fit, so it does not appear in our sample.

JADES-GS-53.19592-27.7555 ($z_a = 15.32$). This slightly extended F150W dropout has S/N > 5 in three filters: F277W, F356W, and F444W. It is also over $3''$ away from any bright sources. Because of the nondetection in F150W, we estimate that $m_{\rm F150W} - m_{\rm F200W} > 0.74$ given a 2σ upper limit on the observed F150W flux.

JADES-GS-53.07557-27.87268 ($z_a = 15.31$). This is one of the faintest $z > 12$ sources ($m_{\rm F277W,Kron} = 30.04$), although it is observed at S/N > 5 in three filters: F277W, F356W, and F444W. In the thumbnail, we show how this candidate is surrounded by other, brighter sources. The sources to the NW and SE are both at $z_a \sim 1.0$, while the source with multiple components to the NE is an F435W dropout at $z_a = 3.74$.

JADES-GS-53.17847-27.75591 ($z_a = 15.13$). This very compact F150W dropout is quite faint ($m_{\rm F277W,Kron} = 29.79$), and is
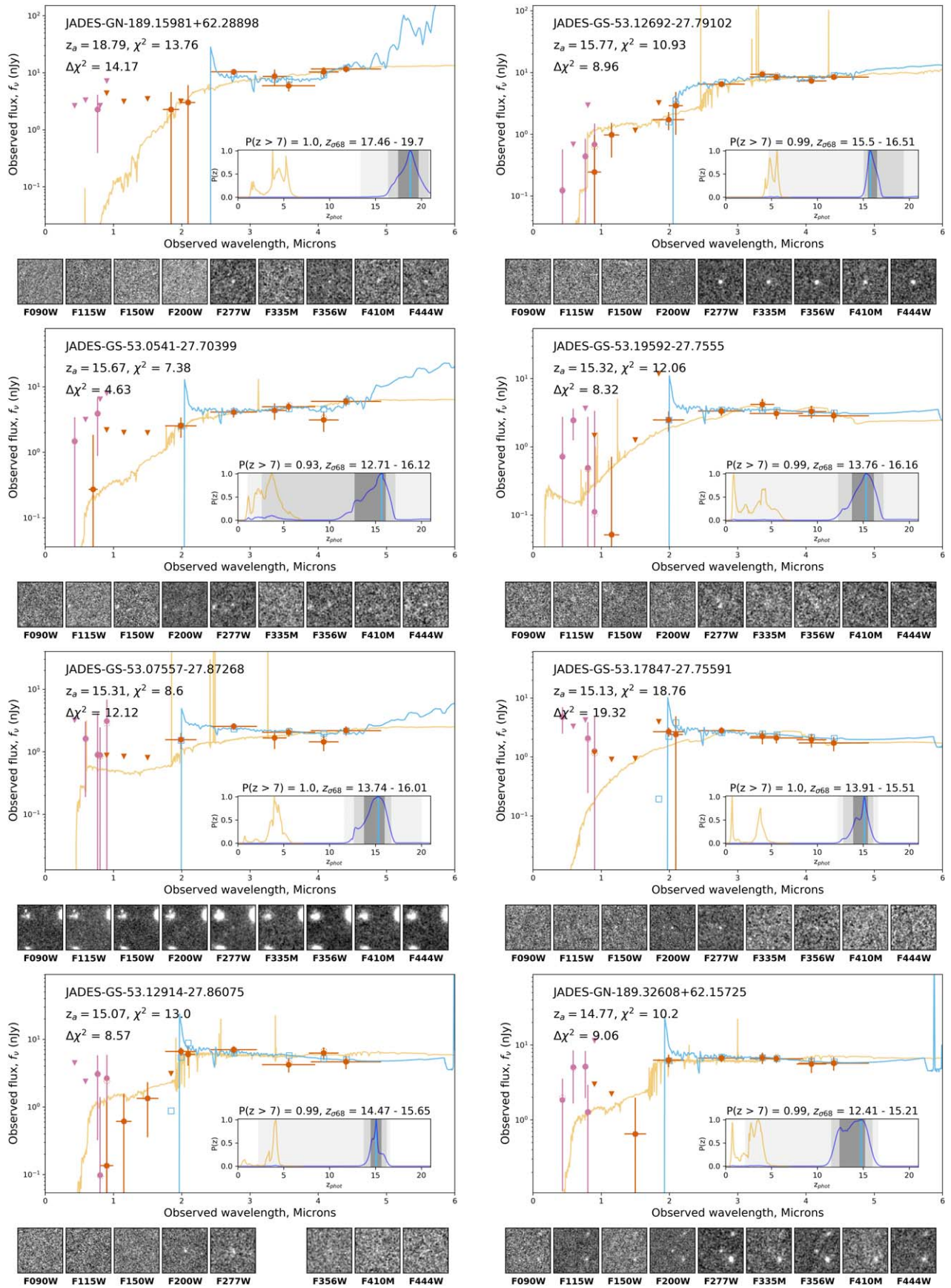
Figure 8. Example SEDs for eight candidate GOODS-S and GOODS-N galaxies at $z_a > 12$. The remainder of the objects are in Figures 18, 19, and 20 in Appendix B. In each panel, the colors, lines, and symbols are as in Figure 2.

relatively isolated, with the nearest bright galaxy being almost $2''$ to the west. The lack of significant detections in the bands to the blue of the proposed Lyα break ($m_{\rm F150W} - m_{\rm F200W} > 1.14$) provides strong evidence of this source's photometric redshift.

JADES-GS-53.12914-27.86075 ($z_a = 15.07$). This F150W dropout is strongly detected (S/N > 7) in F200W and F277W, with $m_{\rm F150W} - m_{\rm F200W} = 1.73$. It is detected at S/N >3 in F210M, but not in F182M.

JADES-GN-189.32608+62.15725 ($z_a = 14.77$). This is an F150W dropout $0''5$ NE of an F850LP dropout galaxy at $z_a = 5.2$, which is a slightly higher redshift than the potential secondary minimum in the $P(z)$ surface for this source. We measure $m_{\rm F150W} - m_{\rm F200W} = 2.46$, and find that this source is still at $z > 12$ within the σ_{68} range on the photometric redshift.

JADES-GS-53.02212-27.85724 ($z_a = 14.59$). This slightly diffuse F150W dropout has S/N > 5 in all of the bands where it is detected, and we measure $m_{\rm F150W} - m_{\rm F200W} = 2.91$. It is near the western edge of the JADES medium mosaic, and is $2''5$ SE of the star GOODS J033205.16-275124.2.

JADES-GN-189.23606+62.16313 ($z_a = 14.47$). This F150W dropout is faint ($m_{\rm F277W,Kron} = 29.40$), but has a 7σ detection in F277W, and a 6σ detection with F356W. We measure a very red dropout color $m_{\rm F150W} - m_{\rm F200W} = 4.28$.

JADES-GS-53.10763-27.86014 ($z_a = 14.44$). This is a faint, diffuse F150W dropout that is within $1''5$ of a larger galaxy at $z_a = 0.9$. While there is evidence of F115W flux in the thumbnail, it is only at a S/N = 1.64.

JADES-GS-53.07427-27.88592 ($z_a = 14.36$). This F150W dropout is not detected at S/N < 0.8 in each of the bands shortward of the potential Lyα break, and we measure $m_{\rm F150W} - m_{\rm F200W} = 4.05$. It is $1''$ away from a F435W dropout at $z_a = 4.31$, and could be associated with that source, as the secondary $P(z)$ peak indicates.

JADES-GN-189.16733+62.31026 ($z_a = 14.33$). This F150W dropout is very bright in F277W ($m_{\rm F277W,Kron} = 27.28$), pushing it above the distribution at these redshifts, as seen in Figure 4. It is within $0''5$ of an F435W dropout at $z_a = 4.34$. As a result, the potential Lyα break for this object could be a Balmer break if these two sources are associated at similar redshifts.

JADES-GS-53.11127-27.8978 ($z_a = 14.22$). This source is an F150W dropout solid S/N > 5 detection in the LW JADES filters. The short-wavelength fluxes for this object may be impacted by detector artifacts which are seen to the NW and SE of the source.

JADES-GN-189.24454+62.23731 ($z_a = 14.0$). This F150W dropout is only detected with >5σ in F277W (S/N = 7.32) and F356W (S/N = 7.08), and we measure $m_{\rm F150W} - m_{\rm F200W} > 0.93$.

JADES-GS-53.06475-27.89024 ($z_a = 14.0$). This F150W dropout ($m_{\rm F150W} - m_{\rm F200W} > 2.27$) is detected in the F277W filter at 19.9σ, and is found in the exceptionally deep GOODS-S JADES 1210 Parallel. In this region, there are no medium-band observations from either JEMS or FRESCO for this source, and we do not see any detection in any of the WFC3 or ACS bands. This source a quite promising high-redshift candidate, with a $\Delta\chi^2 \sim 65$.

JADES-GS-53.14673-27.77901 ($z_a = 13.68$). This F150W dropout is quite well detected in multiple bands, including F182M, but it has a fairly broad $P(z)$ surface, although the σ_{68} values are consistent with $z > 12$ solutions. At $z_{\rm phot} \sim 13-14$,

the fits are more unconstrained due to the widths of the F150W and F200W photometric bands and the gap between them.

JADES-GS-53.14988-27.7765 ($z_a = 13.41$). This source, also known as JADES-GS-z13-0, was spectroscopically confirmed to be at $z_{\rm spec} = 13.20$ in Curtis-Lake et al. (2023), and the NIRCam photometry and morphology for the source was discussed in Robertson et al. (2023). The source is fairly bright ($m_{\rm F200W,Kron} = 28.81$) with a strong observed Lyα break, and the $\sigma68$ range on the photometric redshift ($z_{\sigma68} = 12.92-14.06$) is in agreement with the observed spectroscopic redshift.

JADES-GN-189.27873+62.2112 ($z_a = 13.12$). This source has F182M and F210M fluxes boosted by flux from a diffraction spike. This source has an F150W detection at 2.4σ, potentially demonstrating that it is at a slightly lower redshift, as indicated by the large $P(z)$ distribution.

JADES-GN-189.11004+62.23638 ($z_a = 13.12$). The F182M and F210M fluxes for this F150W dropout ($m_{\rm F150W} - m_{\rm F200W} = 2.69$) are also boosted by a diffraction spike from a nearby star. There appears to be a F115W flux at 2.14σ, but this is shifted to the NE of the primary source by $0''3$ seen in F200W and F277W.

JADES-GS-53.06928-27.71539 ($z_a = 12.69$). This is a faint ($m_{\rm F277W,Kron} = 29.73$) F150W dropout with a very red dropout color $m_{\rm F150W} - m_{\rm F200W} = 4.97$.

JADES-GN-189.33638+62.16733 ($z_a = 12.53$). While this F150W dropout is faint ($m_{\rm F277W,Kron} = 30.01$), the fit indicates a blue UV slope and the object is detected in multiple filters at >5σ, with $\Delta\chi^2 = 12.94$.

JADES-GS-53.18129-27.81043 ($z_a = 12.52$). This very faint ($m_{\rm F277W,Kron} = 30.11$) F150W dropout has solid 8σ detections in F200W and F277W, and can be seen in the F356W thumbnail at 4σ.

JADES-GS-53.08468-27.86666 ($z_a = 12.48$). This F150W dropout ($m_{\rm F150W} - m_{\rm F200W} = 1.96$) has a slightly redder potential UV slope, and this may be a low-redshift dusty interloper.

JADES-GS-53.16635-27.82156 ($z_a = 12.46$). This galaxy, also known as JADES-GS-z12-0, was originally spectroscopically confirmed to lie at $z_{\rm spec} = 12.63$ in Curtis-Lake et al. (2023), and the NIRCam photometry and morphology for the source was discussed in Robertson et al. (2023). Recent, deeper NIRSpec observations for this source showed C III]$\lambda\lambda$ 1907,1909 line emission, indicating a spectroscopic redshift of $z_{\rm spec} = 12.479$ (D'Eugenio et al. 2023). This source is a bright ($m_{\rm F277W,Kron} = 28.64$) F150W dropout ($m_{\rm F150W} - m_{\rm F200W} = 2.01$) with a 26$\sigma$ detection in F277W, and is observed at the 4–6σ level in the relatively shallow F182M and F210M filters.

JADES-GS-53.02868-27.89301 ($z_a = 12.39$). This source is an F150W dropout with strong detections (S/N > 5) in each filter to the red of the potential Lyα break.

JADES-GS-53.10469-27.86187 ($z_a = 12.27$). This source is an F150W dropout with strong detections in F200W and F277W. The fluxes at F115W and F150W are observed at 1.55σ and 1.39σ significance, respectively.

JADES-GN-189.27641+62.20724 ($z_a = 12.19$). This source is well detected in F200W and F277W (S/N > 10 in both filters), but is quite faint at longer wavelengths. There is a source $1''5$ SE of the target at $z_{\rm spec} = 2.44$ (Reddy et al. 2006), so we caution that the observed Lyα break for the high-redshift candidate may be a Balmer break at 1.5 μm.

JADES-GN-189.09217+62.25544 ($z_a = 12.16$). This is a bright ($m_{\rm F277W,Kron} = 28.53$) F150W dropout. The F150W

detection is at a S/N = 2.03, while the F115W flux is only measured at the 1.55σ level.

JADES-GS-53.19051-27.74982 ($z_a = 12.08$). This is a bright ($m_{F277W,Kron} = 28.72$) F115W dropout with multiple filters with $>10\sigma$ detections.

JADES-GS-53.14283-27.80804 ($z_a = 12.06$). This object is an F150W dropout that is primarily seen in F200W (S/N = 5.89) and F277W (S/N = 6.72). The fit very strongly favors the high-redshift solution, and it does not seem be associated with the nearby galaxy to the east, an F814W dropout at $z_a \sim 5.98$ with [O III]λ5007 potentially boosting the F335M flux.

JADES-GS-53.18936-27.76741 ($z_a = 12.05$). This source is a very faint, slightly diffuse F150W dropout. While the $\Delta\chi^2$ is still in favor of the $z > 8$ fit, the lower-redshift solution would help explain the boosted F210M flux as potentially arising from an [O III] emission line, although the F210M flux is only significant at 2.6σ.

We caution that photometric redshifts at $z > 12$ are quite uncertain, and that our sources are observed down to very faint magnitudes, and thus require deep spectroscopic follow-up to confirm. In many cases, we also raise the possibility that the source is potentially associated with a nearby galaxy at lower redshift. For the GOODS-S sources, continued observations extending both the size of the JADES Medium region and the depth of JADES Deep planned for Cycle 2 as part of JADES will help to provide evidence as to whether these sources are truly at high redshift or not.

4.4. z > 8 Candidates with $\Delta\chi^2 < 4$

In the previous sections, we explored those objects for which the EAZY fit strongly favors a high-redshift solution. The fits to these sources at their proposed photometric redshifts indicate strong Lyα breaks and more robust upper limits on the photometric fluxes blueward of the break. For cases where the observed HST/ACS or short-wavelength JWST/NIRCam fluxes have higher uncertainties (for fainter objects or those objects in shallower parts of the GOODS-S or GOODS-N footprint), fits at $z < 7$ are less strongly disfavored, leading to values of $\Delta\chi^2 < 4$.

We selected candidate $z > 8$ galaxies in our sample that satisfy our criteria outlined in Section 3.2, but where $\Delta\chi^2 < 4$. While the bulk of the output EAZY $P(z)$ indicates that the galaxy is at high redshift ($P(z > 7) > 0.7$), the minimum χ^2 for the $z < 7$ solution is more similar to the overall minimum χ^2 at $z > 8$. In this section, we explore these targets, as they represent a not insignificant number of candidates.

Following the initial selection of these objects, they were visually inspected following the same routine as for the $\Delta\chi^2 > 4$ objects, where an object was removed from the sample if the majority of reviewers flagged it for rejection. Our final sample consists of 163 candidates in GOODS-S and 64 candidates in GOODS-N, for a total of 227 objects. These objects are also plotted with lighter symbols in Figure 3. While these sources span the full redshift range of the $\Delta\chi^2 > 4$ sample, the median F277W Kron magnitude is 29.47 for the GOODS-S objects and 29.11 for the GOODS-N objects, fainter than the median F277W magnitudes of the $\Delta\chi^2 > 4$ sources (29.25 for GOODS-S and 28.62 for GOODS-N). This is expected as $\Delta\chi^2$ is strongly dependent on the observed flux uncertainties for each source.

In Figure 9, we highlight some targets from both GOODS-S and GOODS-N with $\Delta\chi^2 < 4$, demonstrating the variety of targets in this subcategory. The median F090W flux (measured in a $0\rlap.{''}2$ diameter aperture) for the full sample of GOODS-S and GOODS-N $z > 8$ candidates is -0.02 nJy (the distribution is consistent with 0 nJy), while the median F090W flux for the combined sample of $\Delta\chi^2 < 4$ targets is 0.39 nJy. Targets like JADES-GS-53.04744-27.87208 ($z_a = 12.33$) and JADES-GN-189.33478+62.1919 ($z_a = 12.38$) have faint F115W and F150W flux measurements (with high uncertainties) consistent with dusty $z \sim 4$ solutions with strong emission lines, similar to CEERS-93316 observed in Arrabal Haro et al. (2023a). Many of these objects are also limited by the lack of deep HST/ACS data; JADES-GS-53.04744-27.87208 only has coverage with F435W and F606W due to its position in the SW of the JADES GOODS-S footprint.

We include these sources and their fluxes to aid in the selection of high-redshift galaxies in future deep JWST surveys with different filter selection and observational depths. While a larger number of these objects may be lower-redshift interlopers masquerading as $z > 8$ galaxies, this sample may serve as a pool of additional sources to be placed on multi-object slit masks in follow-up spectroscopic campaigns to confirm source redshifts. In addition, these objects are helpful with calibrating template sets as they have colors that can be fit with models at low and high redshift.

4.5. z > 8 Candidates Proximate to Brighter Sources

In addition to exploring the sources with $\Delta\chi^2 < 4$, we also looked at objects (at all $\Delta\chi^2$ values) that were near bright sources, being within $0\rlap.{''}3$ or the bounding box of a source with 10 times greater brightness. There is an increased probability that proximate sources are at similar redshifts, and so we can compare the χ^2 distribution of the brighter galaxy to that of the fainter high-redshift candidate. At faint magnitudes, Balmer breaks and strong line emission can lead to sources being mistaken for higher-redshift objects, which can be seen by looking at the χ^2 minima for these sources. In addition, being so close to a bright source can potentially introduce flux into the circular aperture photometry and change the observed colors of the candidate galaxy and the shape of the SED. We went through the same visual classification procedure for these sources as we did for the full sample, and ended up with 41 candidates (30 have $\Delta\chi^2 > 4$) in GOODS-S and 17 candidates (14 have $\Delta\chi^2 > 4$) in GOODS-N. These sources have a median F277W Kron magnitude of $m_{AB} = 28.61$ for those in GOODS-S, and $m_{AB} = 27.50$ for those in GOODS-N, and range in redshift between $z = 8.0$ and 16.7.

We want to specifically highlight some of the higher-redshift candidates from this subsample. Notably, there are three galaxies at $z_a > 12$: JADES-GS-53.08016-27.87131 ($z_a = 16.74$), JADES-GS-53.09671-27.86848 ($z_a = 12.03$), and JADES-GN-189.23121+62.1538 ($z_a = 12.16$). JADES-GS-53.08016-27.87131 has $\Delta\chi^2 < 4$, although this source is the most interesting due to its photometric redshift. This source has a very faint F200W detection (S/N > 4 in an $0\rlap.{''}2$ diameter aperture), but is relatively bright at longer wavelengths (with an F277W AB magnitude of 29.20). This source lies $3''-4''$ north of a pair of interacting galaxies at $z_{spec} = 1.1$ (Bonzini et al. 2012; Momcheva et al. 2016), and flux from the outskirts of these galaxies may be contributing to the aperture photometry for this object, leading to an artificially red UV slope. We caution that this source may be a
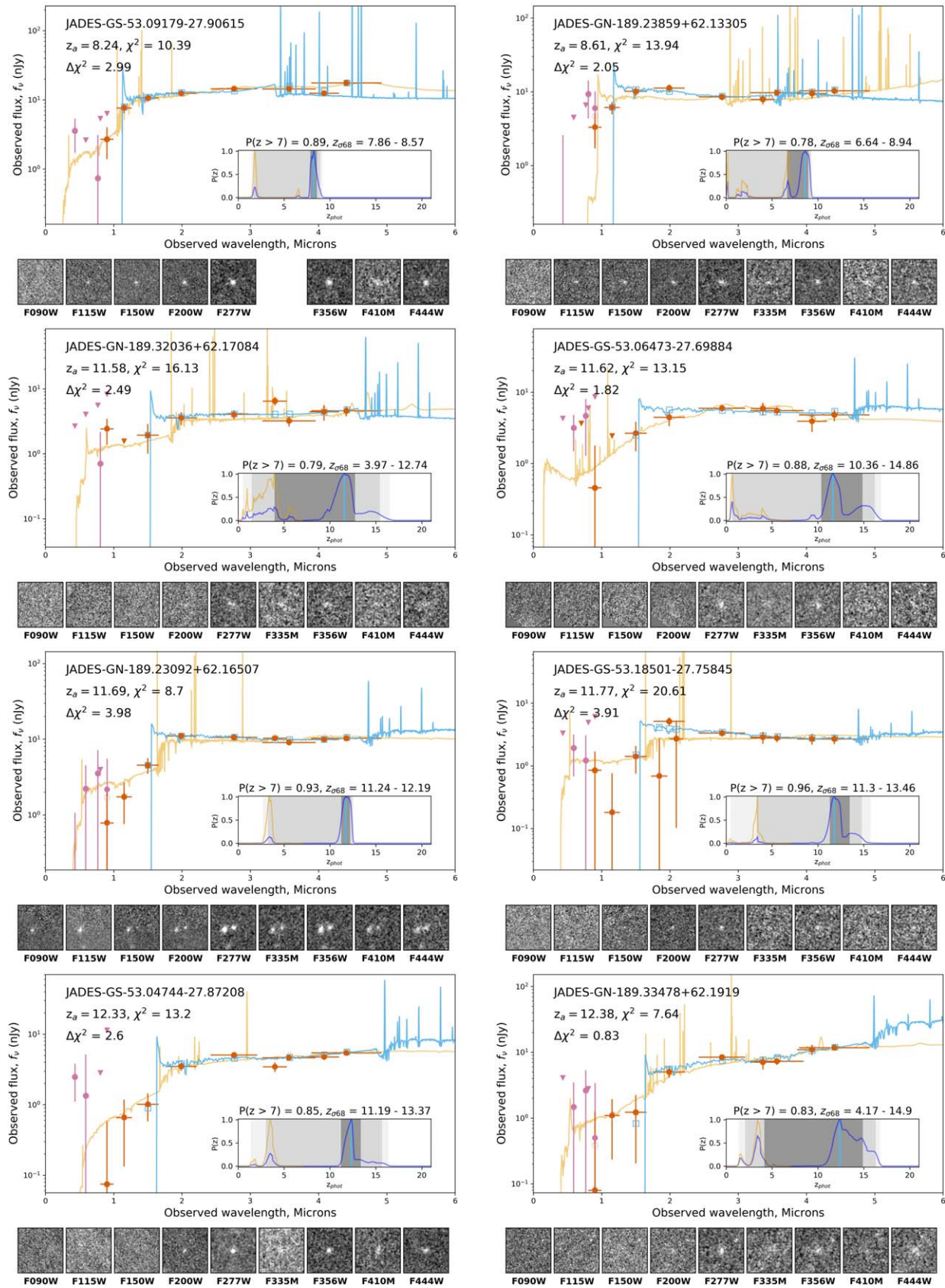
Example $\Delta\chi^2 < 4$ Candidates

Figure 9. Example SEDs for eight $\Delta\chi^2 < 4$ candidate GOODS-S and GOODS-N galaxies. In each panel, the colors, lines, and symbols are as in Figure 2.

stellar cluster associated with this pair or the dusty galaxies that are to the north of its position.

There are five objects in this subsample that have spectroscopic redshifts from FRESCO: JADES-GS-53.12001-27.85645 ($z_a = 8.33$, $z_{spec} = 7.652$), JADES-GS-53.13341-27.83909 ($z_a = 8.18$, $z_{spec} = 8.217$), JADES-GS-53.07688-27.86967 ($z_a = 8.57$, $z_{spec} = 8.270$), JADES-GS-53.10107-27.86511 ($z_a = 8.49$, $z_{spec} = 8.195$), and JADES-GN-189.27457+62.21053 ($z_a = 8.03$, $z_{spec} = 8.015$). These sources have [O III]λ5007 line detections from FRESCO, demonstrating that while this class of sources may be associated with their nearby brighter neighbors, there are possible high-redshift galaxies among them.

4.6. Stellar Contamination

One primary source of contamination for high-redshift galaxy samples are low-mass Milky Way stars and brown dwarfs, which at low temperatures can have near-IR colors similar to high-redshift galaxies. Many studies have explored the selection of these sources from within extragalactic surveys (Ryan et al. 2005; Caballero et al. 2008; Wilkins et al. 2014; Finkelstein et al. 2015; Ryan & Reid 2016; Hainline et al. 2020). Candidate brown dwarfs have been observed in extragalactic surveys, such as GLASS (Nonino et al. 2023). To explore whether our sample contains objects with a high probability of being a possible brown dwarf, we looked at the sizes of the targets in our sample and their fits to stellar models and observed brown-dwarf SEDs.

We fit the targets in our sample using the `jades-pipeline` profile-fitting software, which utilizes the python `lenstronomy` package (Birrer & Amara 2018; Birrer et al. 2021). We fit each source, as well as the other nearby sources within $2''$ and up to two magnitudes fainter than the primary galaxy as a Sersic profile. Objects that are fainter or farther from the source are masked instead of fit. We use the final residuals to determine the goodness of fit for each source. We measured the sizes using the NIRCam F444W mosaic, as brown dwarfs are bright and unresolved at 4 μm (Meisner et al. 2020). To determine whether an object was unresolved, we looked at those where the observed half-light radius for each source was smaller than the NIRCam LW channel pixels size ($0''063$). We note that the maximum half-light radius measured using the same procedure on a sample of stars and brown dwarfs in GOODS-S and GOODS-N was $0''02$, but adopted a larger limit to broaden our search. These sources were identified using both photometric fits to theoretical brown-dwarf models and identification of sources with proper motions compared to HST observations, and will be described further in Hainline et al. (2023).

We fit the NIRCam photometry of our $z > 8$ candidates using both the SONORA cloud-free brown-dwarf models from Marley et al. (2018) as well as a sample of observed brown-dwarf observations from the SpeX Prism Spectral Library.[27] As the SpeX spectra, in general, are only observed to 2.5 μm, we took a group of objects across the temperature range that were detected in the Wide Field Infrared Survey Explorer (WISE) allWISE catalog (Cutri et al. 2021) and used their photometry at 3.4 and 4.6 μm to create an extrapolated spectra out to 5 μm, which we used to estimate NIRCam photometry, following

Finkelstein et al. (2023). We supplemented these with empirical NIRCAM SEDs of M dwarfs, obtained from a selection of extremely compact objects in F115W–F200W color–magnitude space, consistent with stellar evolutionary models and JWST observations of globular clusters (Weisz et al. 2023; B. Johnson, private communication). The full set of model photometry was then fit to the observed NIRCam $0''2$ diameter aperture photometry for the $z > 8$ candidate galaxies using a χ^2 minimization approach. We compared the resulting χ^2 minima for the stellar fits to those from the EAZY galaxy templates, and if an object had a $\Delta\chi^2 < 4$ between the galaxy model fit and the stellar fit, it was flagged as a brown-dwarf candidate.

We find 303 objects in our $z > 8$ sample with $\Delta\chi^2 > 4$ that are unresolved (42% of the full $z > 8$, $\Delta\chi^2 > 4$ sample), with a half-light radius less than $0''063$, while only six objects across both fields have fits to stellar models with EAZY χ^2_{min} within $\Delta\chi^2 < 4$ (two of these sources have lower χ^2 values with the brown-dwarf fits). We flag the sources in the online table if they satisfy either of these requirements. Of these objects, only two sources are both unresolved and have stellar fits within $\Delta\chi^2 < 4$: JADES-GS-53.0353-27.87776 ($z_a = 10.82$) and JADES-GN-189.19772+62.25697 ($z_a = 8.61$). The latter source, which is detected with HST WFC3/IR, was identified as the Y-dropout candidate GNDY-6474515254 in Bouwens et al. (2015). While this object has evidence for being a brown dwarf, FRESCO identified both [O III]$\lambda\lambda$ 5007, 4959 emission lines ($z_{spec} = 8.28$), ruling out the brown-dwarf hypothesis.

There are additional brown-dwarf candidates in the $z > 8$ candidate galaxies with $\Delta\chi^2 < 4$, identified in Section 4.4. We find 83 objects with an F444W half-light radius less than $0''063$, and 17 objects with stellar fits within $\Delta\chi^2 < 4$ (six of these sources have lower χ^2 values with the brown-dwarf fits). We caution that because of the larger flux uncertainties for these objects, it is more likely that models would fit these data with comparable χ^2 values, but we include flags in the online table in these cases. Only five of the sources in this subsample are unresolved with comparable brown-dwarf fits to the EAZY fits: JADES-GS+53.02588-27.87203 ($z_a = 8.84$), JADES-GS +53.12444-27.81363 ($z_a = 8.33$), JADES-GS+53.07645-27. 84677 ($z_a = 8.64$), JADES-GN+189.16606+62.31433 ($z_a = 8.6$), and JADES-GN+189.07787+62.23302 ($z_a = 8.1$). These sources, on visual inspection, do not appear to be strong brown-dwarf candidates due to them being quite faint, which would indicate potentially unphysical distances compared to models of the halo brown-dwarf population (Ryan et al. 2005). While there are 19 unresolved sources in the sample that are proximate to brighter objects (as in Section 4.5), none of these have stellar fits within $\Delta\chi^2 < 4$ of the EAZY fits.

4.7. z > 8 Candidates in the Literature

As the GOODS-S and GOODS-N fields have been observed across a wide wavelength range and to deep observational flux limits, a number of the sources in our sample have been previously presented in the literature. As described in Robertson et al. (2023), both JADES-GS-z10-0 (JADES-GS-53.15883-27.7735) and JADES-GS-z11-0 (JADES-GS-53.16476-27.77463) were previously identified in Bouwens et al. (2011a), as UDFj-38116243 and UDFj-39546284, respectively. Both of these galaxies are in our $z > 8$ sample, as JADES-GS-53.15883-27.7735 and JADES-GS-53.16476-27.77463. Similarly, we also previously discussed GN-z11, first identified in Bouwens et al. (2010) and later further

---

[27] Compiled by Adam Burgasser and found online at http://pono.ucsd.edu/~adam/browndwarfs/spexprism/.

explored in Oesch et al. ([2014](#), [2016](#)), which is present in our sample as JADES-GN-189.10605+62.24205.

In Bouwens et al. ([2023](#)), the authors use the publicly available JEMS data to search for $z > 8$ candidates in GOODS-S and construct a sample of 10 sources. Nine of the 10 sources appear in our sample (their source XDFY-2376346017, which they measure at $z_{EAZY} = 8.3^{+0.2}_{-0.2}$, is at $z_a = 7.89$ in our fits, and we additionally measure a FRESCO $z_{spec} = 7.975$ for this source), and, of those, eight sources were previously known and are in our sample. The remaining two sources were not previously known, and also appear in our sample: JADES-GS-53.13918-27.78273 ($z_a = 10.49$) and JADES-GS-53.16863-27.79276 ($z_a = 11.71$). Donnan et al. ([2023](#)) perform a similar search, and find two additional candidates that fall into our sample: JADES-GS-53.17551-27.78064 ($z_a = 9.66$) and JADES-GS-53.12166-27.83012 ($z_a = 9.42$); they also independently recover JADES-GS-53.16863-27.79276. The photometric redshifts presented in Bouwens et al. ([2023](#)) for JADES-GS-53.13918-27.78273 (XDFH-2334046578 in their sample, $z_{EAZY} = 11.8^{+0.4}_{-0.5}$) and JADES-GS-53.16863-27.79276 (XDFJ-2404647339 in their sample, $z_{EAZY} = 11.4^{+0.4}_{-0.5}$) are broadly similar to our values, but we measure a much lower redshift for the former due to the availability of the F150W flux from JADES. In the same way, Donnan et al. ([2023](#)), estimate similar photometric redshifts to what we find for JADES-GS-53.17551-27.78064 (UDF-21003 in their sample, $z_{phot} = 9.79^{+0.15}_{-0.13}$) and JADES-GS-53.16863-27.79276 (UDF 16748 in their sample, $z_{phot} = 11.77^{+0.29}_{-0.44}$), but they claim a much higher redshift for JADES-GS-53.12166-27.83012 (UDF-3216 in their sample, $z_{phot} = 12.56^{+0.64}_{-0.66}$), which is inconsistent with the measured F150W flux. We note that this latter candidate appears in our catalog of sources proximate to brighter objects, although with $\Delta\chi^2 = 4.32$.

For the full sample of $\Delta\chi^2 > 4$ candidates at $z > 8$, we additionally cross-matched their sky positions against GOODS-S and GOODS-N high-redshift catalogs in the literature, including Bunker & Wilkins ([2009](#)), Bunker et al. ([2010](#)), Yan et al. ([2010](#)), Bouwens et al. ([2011a](#)), Lorenzoni et al. ([2011](#)), Ellis et al. ([2013](#)), Lorenzoni et al. ([2013](#)), McLure et al. ([2013](#)), Oesch et al. ([2013](#)), Schenker et al. ([2013](#)), Oesch et al. ([2014](#)), Bouwens et al. ([2015](#)), Finkelstein et al. ([2015](#)), Bouwens et al. ([2016](#)), Harikane et al. ([2016](#)), and Bouwens et al. ([2021](#)). Because our JADES mosaics were aligned using the Gaia reference frame, we had to carefully visually match against each sample, which have different reference frames. In Table [4](#), we list the targets that were matched to sources previously discussed in the literature, the photometric redshift for these sources, and we include the references for each object.

We find 47 objects across the full $\Delta\chi^2 > 4$ catalog have been discussed previously in the literature, 42 in GOODS-S and five in GOODS-N. As previously mentioned, seven are at $z_a > 10$, three are at $z_a = 9-10$, and the remaining 37 are at $z_a = 8-9$.

4.8. Alternative EAZY Template-fitting Results

In Larson et al. ([2023](#)), the authors present a series of theoretical galaxy templates designed to be used with EAZY to better model the bluer UV slopes expected for very-high-redshift galaxies.[28] To create these templates, the authors first used EAZY to calculate photometric redshifts for mock galaxies

---

[28] https://ceers.github.io/LarsonSEDTemplates

in the CEERS Simulated Data Product V32 catalog using the EAZY "tweak_fsps_QSF_v12_v3" templates, which were derived from fsps. At this point, the authors created an additional set of templates that better matched the simulated $m_{F200W} - m_{F277W}$ colors for the $z > 8$ galaxies in their sample using the binary stellar evolution models BPASS (Eldridge et al. [2017](#)) with nebular emission derived from the spectral synthesis code CLOUDY (Ferland et al. [2017](#)). These templates resulted in significantly better photometric redshift estimations for the mock galaxies with the CEERS filter set.

To explore how our choice of EAZY templates affects our final $z > 8$ sample, we fit the photometry for all of the objects recovered across GOODS-N and GOODS-S with EAZY with the recommended template set from Larson et al. ([2023](#)) for fitting $z > 8$ galaxies: "tweak_fsps_QSF_v12_v3" along with the BPASS-only "Set 1" and the "BPASS + CLOUDY – NO LyA" "Set 4" templates. We ran EAZY in an otherwise identical manner, including the template error function used, but we utilized the same photometric offsets as provided in Table [2](#).

The resulting photometric redshifts for our primary sample of $z > 8$ sources provide no significant differences or noticeably improved photometric redshift fits: Only 4% have $|z_{Larson} - z_a|/(1 + z_a) > 0.15$ (23 sources in GOODS-S and five sources in in GOODS-N). More importantly, if we look at those sources where $z_{Larson} < 8$, only 2.5% (14 sources in GOODS-S and four sources in GOODS-N) have significantly different photometric redshifts. In the majority of these cases, the lower-redshift solution offered by the Larson et al. ([2023](#)) templates is at the same secondary χ^2 minimum seen for our own template fits, and the validity of the fit is strongly dependent on the observed F090W or F115W fluxes.

The sources in our sample with $\Delta\chi^2 < 4$ fits are less robust, as has previously been discussed, and show more discrepancy between the fits with our EAZY templates and those from Larson et al. ([2023](#)). Here, 37% have $|z_{Larson} - z_a|/(1 + z_a) > 0.15$ (67 sources in GOODS-S and 17 sources in GOODS-N). Sixty-four of these GOODS-S sources and 15 of the GOODS-N sources (for a total fraction of 35% of the $\Delta\chi^2 < 4$ objects) have $z_{Larson} < 8$.

In addition, we derived a sample of $z_a > 8$ sources from fits with the Larson et al. ([2023](#)) templates after applying the same S/N, $P(z > 7)$, and $\Delta\chi^2$ cuts as described in Section [3.2](#). We compared the resulting candidates with those from the original template set, and after visual inspection found a total of 10 additional $z > 8$ candidates (seven in GOODS-S and three in GOODS-N), which we list in Table [6](#). Of those sources, five are at $z_a = 6-8$ and two have $P(z < 7) < 0.7$ in our own EAZY fits. The remaining three objects are quite faint, but should be considered alongside the main sample. We conclude that our results would not be significantly improved by using the Larson et al. ([2023](#)) templates.

4.9. Spectroscopic Redshifts

In total, we have spectroscopic redshifts for 42 objects in our sample. As discussed previously, five of the high-redshift galaxies have been spectroscopically confirmed to lie at $z > 10$: JADES-GS-z10-0, JADES-GS-z11-0, JADES-GS-z12-0, JADES-GS-z13-0 (Curtis-Lake et al. [2023](#); D'Eugenio et al. [2023](#)), and GN-z11 (Bunker et al. [2023a](#)). In this section, we discuss the other objects in our sample with spectroscopic confirmation from both JWST NIRSpec and JWST NIRCam grism spectroscopy from FRESCO. We also compare the

Table 4
$\Delta\chi^2 > 4$ Catalog Sources in the Literature

JADES ID	EAZY z_a	Reference(s)
JADES-GS-53.15751-27.76677	8.00	(1, 2, 3, 4, 5, 6, 8, 10, 12, 13, 16)
JADES-GS-53.16415-27.78452	8.02	(8, 10)
JADES-GS-53.13563-27.79185	8.02	(12, 16)
JADES-GN-189.27457+62.21053[a]	8.03	(12)
JADES-GS-53.08174-27.89883	8.04	(15)
JADES-GS-53.13849-27.85854	8.04	(12, 16)
JADES-GS-53.148-27.79571	8.04	(4, 10, 12, 15, 16)
JADES-GS-53.06029-27.86353	8.04	(12, 13, 16)
JADES-GS-53.17727-27.78011	8.08	(8, 12, 15, 16)
JADES-GS-53.13675-27.83746	8.13	(13)
JADES-GS-53.08745-27.81492	8.17	(7, 12, 16)
JADES-GS-53.06035-27.86355	8.17	(12, 13, 16)
JADES-GS-53.07052-27.86725	8.21	(12, 16)
JADES-GS-53.05924-27.8353	8.22	(12, 16)
JADES-GS-53.1459-27.82279	8.23	(8)
JADES-GS-53.13569-27.83884	8.24	(13)
JADES-GN-189.2032+62.24245	8.28	(12)
JADES-GS-53.14585-27.82274	8.28	(8)
JADES-GS-53.10393-27.89059	8.35	(12, 16)
JADES-GS-53.20988-27.77928	8.36	(12, 16)
JADES-GN-189.09186+62.25744	8.38	(12)
JADES-GS-53.1571-27.83708	8.39	(12, 15, 16)
JADES-GS-53.08738-27.86033	8.46	(8, 12, 13, 16)
JADES-GS-53.10224-27.85925	8.46	(12)
JADES-GS-53.16447-27.80218	8.50	(4, 6, 8, 9, 13, 16, 19)
JADES-GS-53.0865-27.8592	8.50	(12, 16)
JADES-GS-53.08741-27.8604	8.51	(8, 12, 13, 16)
JADES-GS-53.15891-27.76508	8.52	(1, 2, 3, 4, 5, 6, 8, 9, 10, 12, 13, 16, 19)
JADES-GS-53.08932-27.8727	8.53	(8, 13)
JADES-GS-53.1777-27.78478	8.53	(6, 8, 9, 19)
JADES-GS-53.07581-27.87938	8.55	(8, 12, 13, 16)
JADES-GS-53.15784-27.76271	8.57	(12, 16)
JADES-GN-189.19772+62.25697	8.61	(12, 13, 16)
JADES-GS-53.16767-27.80017	8.64	(9, 12, 14, 16, 19)
JADES-GS-53.16337-27.77569	8.65	(6, 8, 9, 10, 12, 16, 19)
JADES-GS-53.15342-27.77844	8.81	(10)
JADES-GN-189.2114+62.1703	8.92	(12, 16)
JADES-GS-53.13363-27.84499	9.36	(14, 16)
JADES-GS-53.12166-27.83012[a]	9.42	(20)
JADES-GS-53.17551-27.78064	9.66	(20)
JADES-GS-53.13918-27.78273	10.49	(19)
JADES-GS-53.15883-27.7735[b]	10.84	(6, 9, 12, 14, 16, 17, 18, 19, 20)
JADES-GN-189.10604+62.24204[c]	11.00	(11, 12, 14, 16)
JADES-GS-53.16863-27.79276	11.71	(19, 20)
JADES-GS-53.16476-27.77463[d]	12.31	(6, 8, 17, 18, 19, 20)
JADES-GS-53.16635-27.82156[e]	12.46	(17, 18, 21)
JADES-GS-53.14988-27.7765[f]	13.41	(17, 18)

Notes.
[a] Proximate to a brighter source, as described in Section 4.5.
[b] JADES-GS-z10-0.
[c] GN-z11.
[d] JADES-GS-z11-0.
[e] JADES-GS-z12-0.
[f] JADES-GS-z13-0.

References. (1) Bunker & Wilkins (2009), (2) Bunker et al. (2010), (3) Yan et al. (2010), (4) Bouwens et al. (2011a), (5) Lorenzoni et al. (2011), (6) Ellis et al. (2013), (7) Lorenzoni et al. (2013), (8) McLure et al. (2013), (9) Oesch et al. (2013), (10) Schenker et al. (2013), (11) Oesch et al. (2014), (12) Bouwens et al. (2015), (13) Finkelstein et al. (2015), (14) Bouwens et al. (2016), (15) Harikane et al. (2016), (16) Bouwens et al. (2021), (17) Curtis-Lake et al. (2023), (18) Robertson et al. (2023), (19) Bouwens et al. (2023), (20) Donnan et al. (2023), (21) D'Eugenio et al. (2023).

photometric redshifts to the spectroscopic redshifts and discuss the observed offset between the two values. Four additional GOODS-S sources have NIRspec spectroscopic redshifts at $z > 8$. Besides GN-z11, there are no GOODS-N NIRSpec

spectroscopic redshifts for our sample. An additional 28 sources in our sample have FRESCO spectroscopic redshifts, with 19 objects in GOODS-S and eight in GOODS-N. As described in Section 4.5, there are four additional GOODS-S
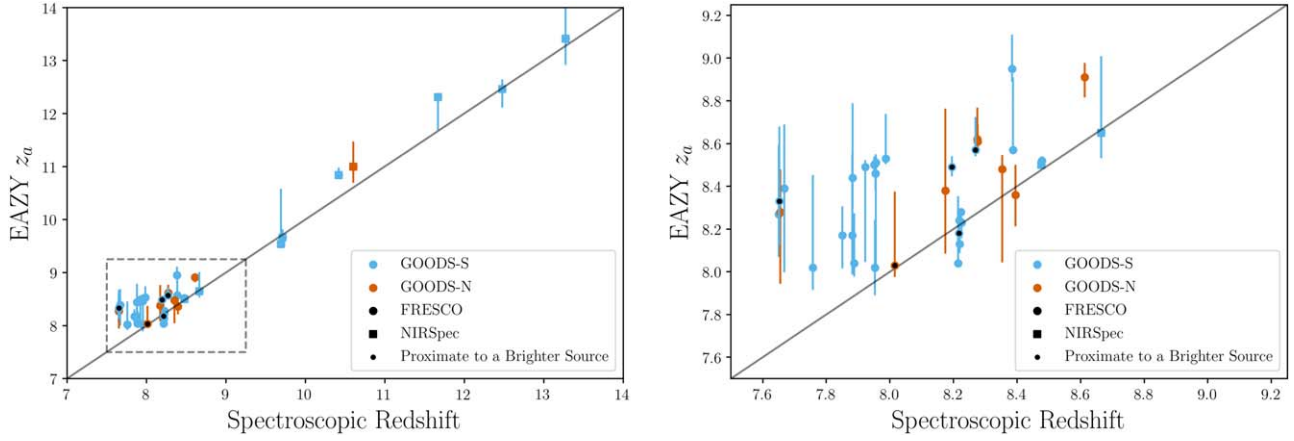
Figure 10. Left: spectroscopic redshifts for objects in our sample measured from both NIRSpec (square symbols) and FRESCO (circular symbols) spectroscopy, as compared to the EAZY photometric redshifts. We highlight those four sources proximate to brighter sources, as discussed in Section 4.5, with black filled circles. Right: a zoom in on the dashed region at $z = 7-9$ in the left panel. We find that the estimated photometric redshifts overpredict the spectroscopic redshifts ($\langle \Delta z = z_a - z_{spec} \rangle = 0.26$), potentially due to the differences between our adopted templates and high-redshift galaxies. We explored removing Lyα emission in our template set, and this lowers the offset to $\langle \Delta z = z_{spec} - z_a \rangle = 0.19$.

sources and one GOODS-N object with FRESCO z_{spec} that are proximate to other bright sources. The photometric redshifts for these sources were derived from either single [O III]λ5007 line detections or, in some brighter cases, multiple line detections. Fifteen of the sources in our sample of $z > 8$ candidates have FRESCO spectroscopic redshifts at $z < 8$ (13 in GOODS-S and one in GOODS-N) in all cases at $z_{spec} > 7.6$. We chose to include these objects as they satisfy our EAZY selection criteria.

In Figure 10, we show the spectroscopic redshifts of the objects in our sample against their photometric redshift. There are no catastrophic outliers, defined here as those objects where $|z_{spec} - z_a|/(1 + z_{spec}) > 0.15$. As discussed previously with individual objects, the photometric redshifts have a systematic offset such that EAZY is slightly overpredicting the distances to these galaxies ($\langle \Delta z = z_a - z_{spec} \rangle = 0.26$). To estimate the scatter on the relationship, we also calculated the normalized mean absolute deviation, σ_{NMAD}, defined as

$$\sigma_{NMAD} = 1.48 \times \text{median}\left(\left| \frac{\delta z - \text{median}(\delta z)}{1 + z_{spec}} \right| \right), \quad (1)$$

where $\delta z = z_{spec} - z_{phot}$. For all of our sources with spectroscopic redshifts, $\sigma_{NMAD} = 0.05$. Understanding the source of this offset is quite important given the usage of photometric redshifts in deriving statistical parameters like the UV luminosity function. By constraining the EAZY fit for each of these sources to be at the spectroscopic redshift, we find that the primary reason for these higher-redshift fits is due to the flux of the filter that spans the Lyα break. In the fits where redshift is constrained to be at z_{spec}, the observed fluxes in the band at the Lyα break are overestimated in the template fits. While this effect may be due to photometric scatter upwards in those bands, it is more likely due to the templates themselves. In Arrabal Haro et al. (2023b), the authors present $z_{spec} = 8-10$ objects with NIRSpec spectroscopy which show a larger offset ($\langle \Delta z = z_a - z_{spec} \rangle = 0.46 \pm 0.11$) to higher photometric redshifts, and these authors also hypothesize that this might be a result of potential differences between the observed high-redshift galaxy SEDs and the templates used to model high-redshift galaxies.

One potential source of excess flux in the UV is the strength of the Lyα emission line in our templates. To explore the effect of this line, we first took our EAZY templates and removed the Lyα contribution by cutting out the flux between 1170 to 1290 Å and replacing that portion in each template with a linear fit. Using these templates without Lyα, we refit every one of our sources with spectroscopic redshifts, and calculated a new $\sigma_{NMAD} = 0.02$, as well as a difference in the average offset $\langle \Delta z = z_a - z_{spec} \rangle = 0.19$. While this is smaller, the offset is still present, indicating that Lyα flux is not the dominant factor. One alternative possibility is that the strength of the optical emission lines at long wavelength may not be fully reflected in our limited template set, and for those $z_{spec} < 9$ sources (where the optical emission is not redshifted out of the NIRCam filters), this may have an effect of pushing fits at higher redshifts. At the redshift range of our sample, the FRESCO redshifts are calculated preferentially for those objects with strong line emission, which may not be probed by our template set. Understanding this offset may prove important for future fits to high-redshift galaxies, and it will necessitate the creation of templates derived from high-resolution NIRSpec spectra of these sources once larger samples are observed.

4.10. Rejected High-redshift Candidates

Finding and characterizing high-redshift galaxies is a complex process, even given the IR filters on board JWST. In our visual inspection, we found a number of bright galaxies that we rejected from our $z > 8$ sample because of multiple reasons. In this section, we will provide four examples as case studies to demonstrate the sorts of galaxies with colors that can mimic those of high-redshift galaxies. This analysis follows discussions in Naidu et al. (2022) and Zavala et al. (2023), and seen directly with CEERS-93316, a candidate galaxy at $z_{phot} = 16.4$ which was shown to be at $z_{spec} = 4.912$ (Arrabal Haro et al. 2023a).

In Figure 11, we provide SEDs for JADES-GS-53.0143-27.88355, JADES-GS-53.08294-27.85563, JADES-GS-53.20055-27.78493, and JADES-GN-189.30986+62.20844. Here, we highlight the solution at $z < 7$ in each, while also leaving the overall minimum χ^2 solution.

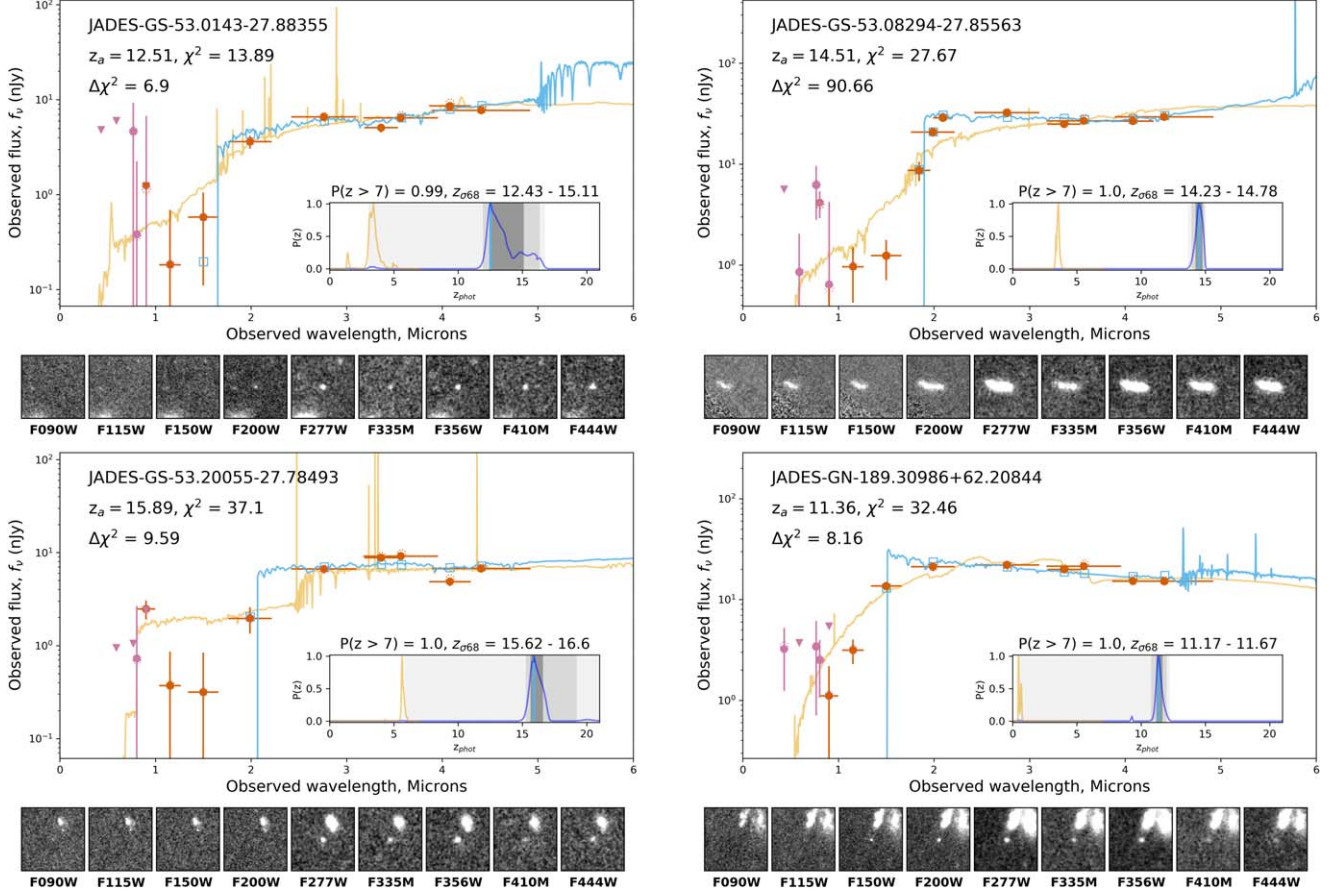## Example Visually Rejected Candidates

Figure 11. Example SEDs for four rejected GOODS-S and GOODS-N galaxies. In each panel, the colors, lines, and symbols are as in Figure 2.

JADES-GS-53.0143-27.88355 ($m_{Kron,AB} = 29.3$). This appears from the thumbnails and from the EAZY minimum χ^2 fit to be an F150W dropout at $z_a = 12.51$. However, the red UV slope indicates that perhaps this object is much dustier and at low redshift ($z_{alt} = 3.41$), where the Hα emission line was boosting the observed F277W flux. This UV slope could also arise from the bright source to the SE (at $z_{spec} = 0.2472$; Cooper et al. 2012). In addition, there is what appears to be a flux detection in the F115W thumbnail, which helps to rule out the high-redshift solution.

JADES-GS-53.08294-27.85563 ($m_{F277W,Kron} = 26.8$). This appears to be a bright F150W dropout clump immediately adjacent to another object. The SED is well fit at $z_a = 14.51$, and the fit constrained to be at $z < 7$ is significantly worse ($z_{alt} = 3.56$). The secondary source, which is detected with all five of the JADES HST/ACS bands (although only at 2σ significance for F435W), has an EAZY template redshift $z_a = 3.4$. This redshift puts the Balmer break between the NIRCam F150W and F200W filters, and we cannot rule out the possibility that this is what we are observing for JADES-GS-53.08294-27.85563. This source appeared in a sample of "HST dark" galaxies in Williams et al. (2023a), where they present a photometric redshift of $z_{phot} = 3.38$, although they use a larger aperture for measuring photometry, which may introduce flux from the nearby source. JADES-GS-53.08294-27.85563 was further imaged in six NIRCam medium-band filters as part of the JWST Cycle 2 GO observations of the JADES Origins Field (PID 3215; Eisenstein et al. 2023b); a more detailed

analysis of this source will be presented in a forthcoming paper from the collaboration (Robertson et al. 2023). Both sources will be observed by the NIRSpec prism in JWST GTO program 1287 (C. Willott 2024, in preparation).

JADES-GS-53.20055-27.78493 ($m_{F277W,Kron} = 28.8$). This appears to be an F200W dropout at $z_a = 15.89$ SE of another, brighter source. While positive flux is observed at the 1–2 nJy level in F115W and F150W, this is at a S/N < 0.8 in both cases. This source was ruled out as an F200W dropout because of the detection at 4σ of the F090W flux, which can be seen in the thumbnail.

JADES-GN-189.30986+62.20844 ($m_{F277W,Kron} = 27.4$). This is best fit at $z_a = 11.36$, placing the observed Lyα break at 1.5 μm. This object is proximate to another, brighter galaxy with an EAZY fit at $z_a = 1.87$ with a complex morphology first observed as part of the GOODS survey in Giavalisco et al. (2004). This is at a lower redshift than the alternative EAZY result for JADES-GN-189.30986+62.20844, $z_a = 2.58$, but the faint F115W detection (S/N = 3.64) demonstrates that the minimum χ^2 redshift solution for this object is erroneous.

5. Discussion

In this section, we explore the selection and derived properties of this large sample of candidate high-redshift galaxies in more detail. A full description of the theoretical implications of these sources is outside the scope of this paper. The stellar mass and star formation histories for these sources
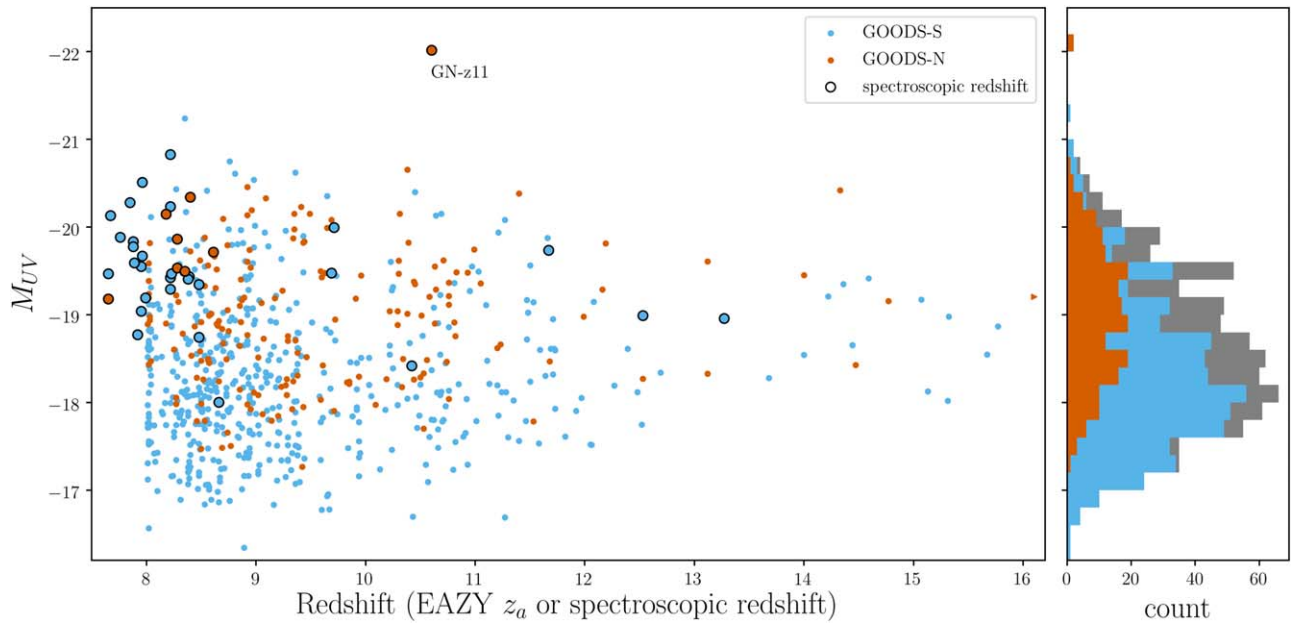
Figure 12. M_{UV} plotted against the best-fitting EAZY z_a photometric redshift or the observed spectroscopic redshift for the $z > 8$ galaxies and candidate galaxies in the GOODS-S (blue) and GOODS-N (red) $z > 8$ samples. The points and colors are the same as Figure 4. On the right, we show the UV magnitude distribution. GN-z11 stands out for its extreme M_{UV}.

will be the focus of a study by S. Tacchella et al. (2024, in preparation), while the full estimation of the evolution of the UV luminosity function at $z > 8$ from the JADES sources will be presented in L. Whitler et al. (2024, in preparation).

5.1. UV Magnitudes

We calculated the UV magnitudes from the EAZY fits to explore the range of intrinsic UV brightnesses for the sample. To calculate M_{UV}, we started by fitting the Kron magnitude catalog fluxes forced to be at the redshifts derived from the smaller circular apertures, or, if available, the spectroscopic redshifts for each source. This was done to not bias the resulting UV magnitudes against more extended objects by encompassing more of the total flux. From here, we took the best-fitting rest-frame EAZY template for each object and passed it through a mock top-hat filter centered at 1500 Å with a width of 100 Å, and calculated the intrinsic UV magnitude based on the resulting flux.

In Figure 12, we show the resulting M_{UV} values against the photometric and spectroscopic redshift for the sample. As can be expected, GN-z11 is by far the brightest source in the sample at $M_{UV} = -22.0$.[29] Excitingly, we find 227 objects in our sample with $M_{UV} > -18$, and 16 objects (all in GOODS-S) with $M_{UV} > -17$, entirely at $z_a < 11.5$. These UV-faint high-redshift galaxy candidates demonstrate the extraordinary depth of the JADES survey. In addition, these results stand in contrast to the decline in the number counts of HST-observed galaxies discussed in Oesch et al. (2018) and Bouwens et al. (2019), and

help to confirm results from other JWST surveys (Finkelstein et al. 2023; Harikane et al. 2023; Pérez-González et al. 2023).

5.2. Dropout Colors

As discussed in the Introduction (Section 1), traditionally, high-redshift samples are assembled by targeting Lyα dropout galaxies in color space. In Hainline et al. (2020), the authors used the JAGUAR mock catalog (Williams et al. 2018) to explore the NIRCam colors of simulated dropout samples, and demonstrated the trade-off between sample completeness and accuracy for high-redshift dropout galaxies. Because of the utility of dropout selection, we sought to explore how successful this technique alone would be at finding the JADES $z > 8$ candidate galaxies. We utilized a uniform two-color selection scheme to target F090W, F115W, and F150W dropouts within our primary $z > 8$ sample, where in each case the color limit for the filters that targeted the Lyα break was $m_1 - m_2 > 1.0$, while the color limit for the filters that targeted the rest-frame UV was $m_2 - m_3 < 0.5$.

In Figure 13, we show the F090W, F115W, and F150W color selection in the top row plots, targeting the entire $z > 8$ sample in each panel. In the bottom panel, we show a photometric redshift histogram for the sources in the sample with a thick gray line, and in the shaded regions the F090W, F115W, and F150W dropout sample distributions. We sum these distributions and plot that with a thick black line. The lone F090W dropout at $z_a > 15$ is JADES-GS-53.12692-27.79102, which we discuss in Section 4.3 and plot in the upper-right panel of Figure 8. We find that 71% of the $z > 8$ sample would be selected as dropouts with these color criteria, while 171 GOODS-S and 37 GOODS-N objects in the sample are not selected by any scheme, which are predominantly at $z \sim 8.5$ and $z \sim 11.5$, as seen from the bottom panel of the figure. These candidates have colors just outside of the selected color space, where $z \sim 8.5$, while $m_{F090W} - m_{F115W} > 1.0$ and $m_{F115W} - m_{F150W} = 0.5-1.0$. A similar effect is seen for the F115W and F150W dropouts at $z \sim 11.5$. This effect could be
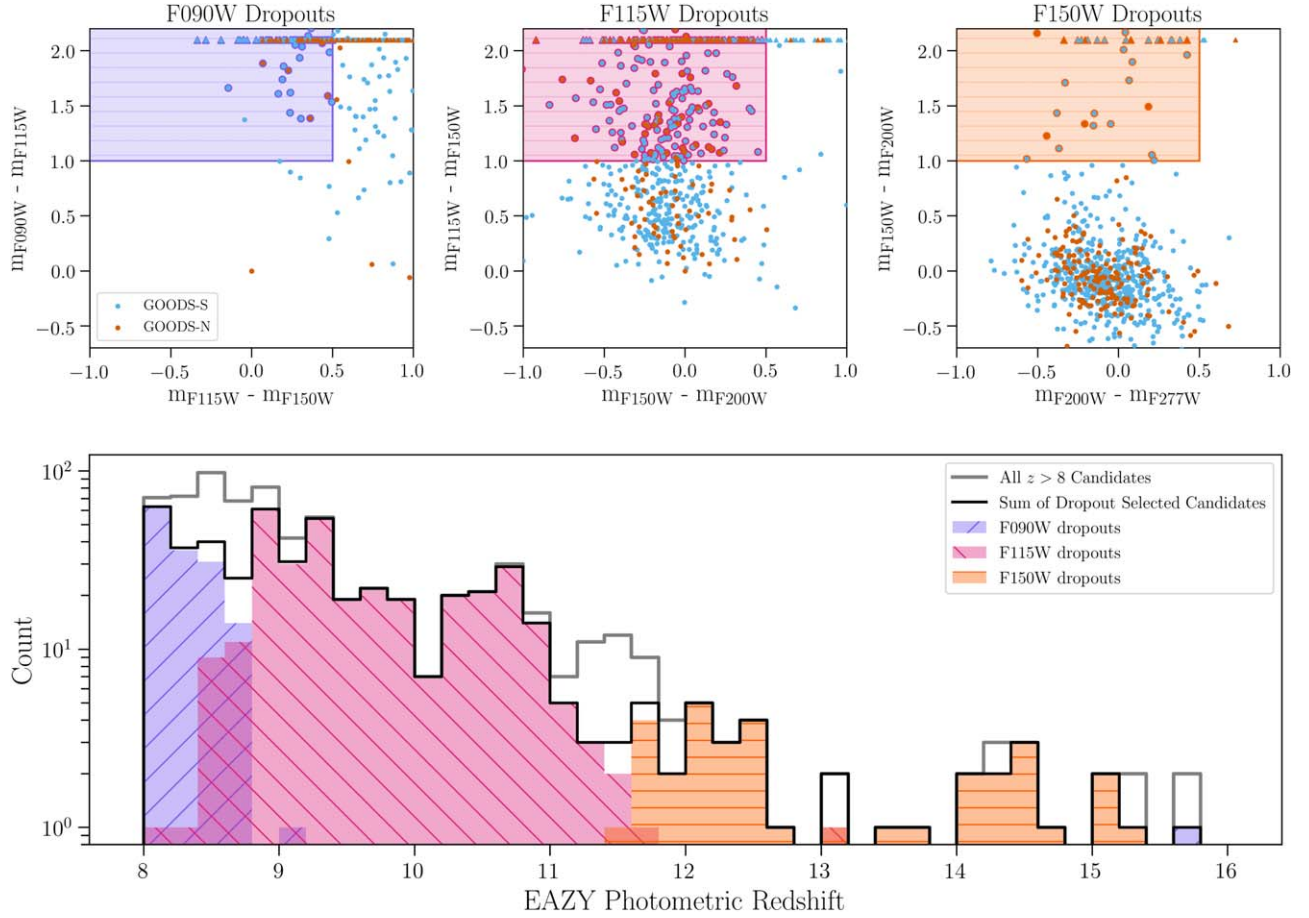
---

[29] In Bunker et al. (2023a), the authors calculate $M_{UV} = -21.5$ for GN-z11 from JWST/NIRSpec spectroscopy for the source, and in Tacchella et al. (2023) the authors present a value of $M_{UV} = -21.6$ from the ForcePho fits to the NIRCam photometry to the source. Our value is higher due to the fact that we estimated M_{UV} from the Kron magnitudes to the source, which includes excess flux from a "haze" observed near the source (Tacchella et al. 2023). The Kron fluxes we use are ~ 1.5 times brighter than what are presented in Tacchella et al. (2023), and if we scale our fluxes by this amount our value changes to $M_{UV} = -21.58$ for GN-z11.

Figure 13. Top row: F090W, F115W, and F150W color-selection diagrams for the GOODS-S and GOODS-N $z > 8$ sample. We show all of the sources in each panel, with upward-pointing arrows plotted for those whose colors place them off the top of each figure. The colored region indicates the simple dropout selection in each panel, and we indicate which sources are selected with thick lines around the symbol. Bottom row: photometric redshift distribution for the $z > 8$ sample plotted with a thick gray line, with the photometric redshifts for each color-selected samples overplotted in colored regions. In black, we plot the sum of all three of the dropout distributions. While the F090W, F115W, and F150W dropouts broadly map to photometric redshifts of $z = 8-8.5$, $z = 8.5-11.5$, and $z = 11.5-15$, respectively, there are a large number of sources in our sample that would not be selected via color selection, as seen by comparing the black and gray histograms.

mitigated by expanding the selection criteria, but this is at the risk of including significantly more lower-redshift interlopers (Hainline et al. 2020).

Another way of looking at color selection is by directly plotting the dropout color against the EAZY photometric redshift. At $z_{\rm phot} = 8$, the Lyα break is at ~ 1.1 μm, which is on the blue edge of the NIRCam F115W band, and by $z_{\rm phot} = 10$, the Lyα break should sit between the F115W and F150W filters, so for the objects at increasing photometric redshifts in this range the F115W S/N will vary as the galaxy's rest-frame UV emission drops out of this band. In Figure 14, we plot the $m_{\rm F115W} - m_{\rm F150W}$ color against the EAZY z_a value for the GOODS-N and GOODS-S objects at $z_{\rm phot} = 8-10$. As expected, the $m_{\rm F115W} - m_{\rm F150W}$ color increases in this redshift range. We find that 95% of the candidate high-redshift galaxies selected as F115W dropouts by our cuts have $z_a > 8.75$, while 16% of the candidates at $z_a = 8.75-10.0$ in our sample would still fall outside of this simple color cut.

5.3. Using $\Delta\chi^2$ to Discern between High- and Low-redshift Template-fitting Solutions

Fitting a galaxy's SED with templates or stellar population synthesis models enables a measurement of the probability of a galaxy being at a range of photometric redshifts. In this study,
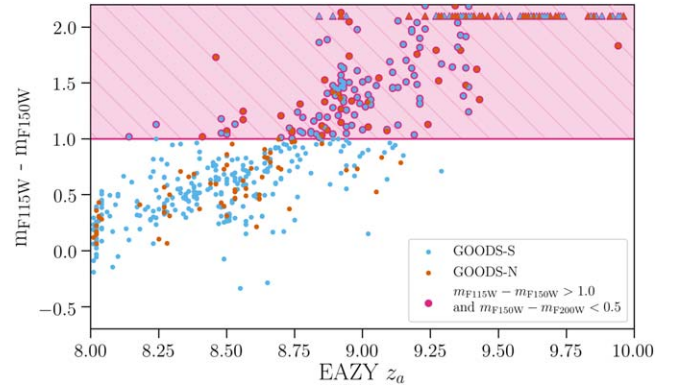
Figure 14. $m_{\rm F115W} - m_{\rm F150W}$ color, as measured using $0\rlap{.}{''}2$ diameter aperture photometry, plotted against the best-fitting EAZY z_a photometric redshift for the GOODS-S (blue) and GOODS-N (red) samples. As photometric redshift increases, the effect of the Lyα break can be seen in the redder $m_{\rm F115W} - m_{\rm F115W}$ color. We shade the region and highlight those objects selected by a $m_{\rm F115W} - m_{\rm F150W} > 1.0$ and $m_{\rm F150W} - m_{\rm F200W} < 0.5$ color cut with a thick outline around the point.

we have used the difference in χ^2 values between the best-fit model and the model constrained to be at $z < 7$ as our metric of accuracy. The exact $\Delta\chi^2$ value we measure for each object is dependent on the template set used, as well as the flux

Table 5
Sources with Red Long-wavelength Slopes

JADES ID	EAZY z_a	m_{F444W}	$m_{F277W} - m_{F444W}$	$m_{F200W} - m_{F356W}$
JADES-GN-189.05064+62.27935	8.04	27.63	1.495	0.209
JADES-GS-53.04601-27.85399	8.3	26.44	1.493	0.602
JADES-GS-53.19904-27.77207	8.31	29.14	1.313	0.182
JADES-GS-53.19211-27.75252	8.53[a]	26.79	1.354	0.608
JADES-GN-189.18036+62.28851	8.69	28.42	1.51	1.021
JADES-GS-53.18392-27.78691	8.71	28.14	1.76	0.907
JADES-GS-53.1387-27.79248	8.87	28.4	1.88	0.475
JADES-GN-189.17121+62.21476	8.91[b]	26.41	1.514	0.535
JADES-GS-53.18354-27.77014	8.95[c]	27.04	1.529	0.506
JADES-GS-53.18087-27.80577	9.33	29.42	1.414	0.185
JADES-GS-53.18448-27.79696	9.66	28.8	1.355	1.783
JADES-GS-53.11023-27.74928	11.64	28.52	1.339	0.372

Notes.
[a] $z_{spec} = 7.99$.
[b] $z_{spec} = 8.62$.
[c] $z_{spec} = 8.38$.

uncertainties and, in our case, the template error function and photometric offsets used. As a result, as is the case for any continuous value of merit, choosing a specific cut is a trade-off between sample accuracy and completeness.

In Harikane et al. (2023), the authors discuss that $\Delta\chi^2 > 4$, the value we adopt in this current work (following Bowler et al. 2020; Harikane et al. 2022; Donnan et al. 2023; Finkelstein et al. 2023) is not sufficient for properly removing low-redshift interlopers, through injecting and recovering mock galaxies in the CEERS extragalactic data. Instead, these authors recommend the stricter cut of $\Delta\chi^2 > 9$. Because we have a larger number of observed photometric filter in the JADES data, choosing a low $\Delta\chi^2$ limit may be resulting in the inclusion of more potential interlopers, which has led to our releasing output catalogs that include all of the sources we visually inspected regardless of the chosen $\Delta\chi^2$ cut.

If we do instead look only at those objects in our sample with $\Delta\chi^2 > 9$, our primary sample is reduced to 483 candidates (358 in GOODS-S and 125 in GOODS-N), or 67% of the 717 $\Delta\chi^2 > 4$ sources (67% in GOODS-S and 69% in GOODS-N). This subsample selected with a stricter cut has a similar redshift distribution to our full sample (19 of the 33 candidates at $z > 12$ would still be included), but the sources have brighter F277W magnitudes, as would be expected. The median F277W magnitude for the $\Delta\chi^2 > 4$ sample is 29.11, while the median F277W magnitude for the $\Delta\chi^2 > 9$ sample is 28.96. It should be noted that every source in our sample with a spectroscopic redshift has $\Delta\chi^2 > 13$. Pushing the cut to even stricter values, we find that 45% of the original sample has $\Delta\chi^2 > 15$ and 36% of the original sample has $\Delta\chi^2 > 20$.

5.4. Candidate Galaxies with Red Long-wavelength Slopes

In our visual inspection of the galaxy candidates, we find a number of high-redshift candidates with very red long-wavelength slopes, following the discovery of similar sources at $z_{phot} = 5-9$ in Akins et al. (2023), Barro et al. (2023), Endsley et al. (2023), Furtak et al. (2023), Labbé et al. (2023), Leung et al. (2023), and Williams et al. (2023a). These objects are often very bright and unresolved in F444W, and in many cases are comparatively faint at shorter wavelengths. To systematically search for these sources in our full sample, we selected those objects that have $m_{F277W} - m_{F444W} > 1.3$ and

$m_{200W} - m_{F356W} > 0.0$. These color limits ensure that the observed red long-wavelength slope is not due to an emission line boosting the F444W flux, and return sources similar to those presented in the literature.

For our sample, these cuts select 12 objects (nine in GOODS-S and three in GOODS-N). Of those sources, 11 are at $z_a = 8-10$, while one source is at $z_a = 11.64$. We provide the IDs, z_a values, F444W magnitudes (measured in an 0″.2 aperture), and colors for these sources in Table 5, and we show six of these sources in Figure 15. Outside of the highest-redshift source, JADES-GS-53.11023-27.74928, these sources have fairly tight lower limits on their redshift due to both the lack of flux observed in the F090W band and the red slope not being easily reproduced at low redshift. The EAZY templates used in the present analysis are able to fit the observed SEDs as high-redshift sources, as is demonstrated with the blue lines in Figure 15. However, JADES-GS-53.11023-27.74928 is very faint ($\sim$1 nJy) at wavelengths shorter than 2 μm, making a photometric redshift estimate difficult. JADES-GS-53.18354-27.77014, a source with a FRESCO spectroscopic redshift ($z_{spec} = 8.38$), is extended with three visible clumps spanning 0″.6 (2.9 kpc at $z_a = 8.38$), of which the central knot has a very observed red UV through optical slope.

The origin of these sources is not obvious. One possible cause of such a red slope is the presence of a dust-obscured accretion disk from supermassive black hole growth in these objects, as discussed in Barro et al. (2023), Furtak et al. (2023), and Akins et al. (2023). This would be of interest given the lack of ultra-high-redshift active galaxies currently known, and the short timescales by which these supermassive black holes could have grown in the early Universe. Another alternative is that these sources could have strong optical line emission that boosts the long-wavelength flux, similar to what is presented in Endsley et al. (2023). In this work, the authors describe how galaxy models with young stellar populations or supermassive black hole growth can replicate the photometry for a sample of sources selected from JWST CEERS. An alternative view is offered in Labbé et al. (2023), who argue that sources like these are instead very massive, and the red long-wavelength slope is indicative of an evolved population, although this interpretation is in contrast to theoretical models of galaxy growth (Prada et al. 2023). A continued exploration of the stellar properties of

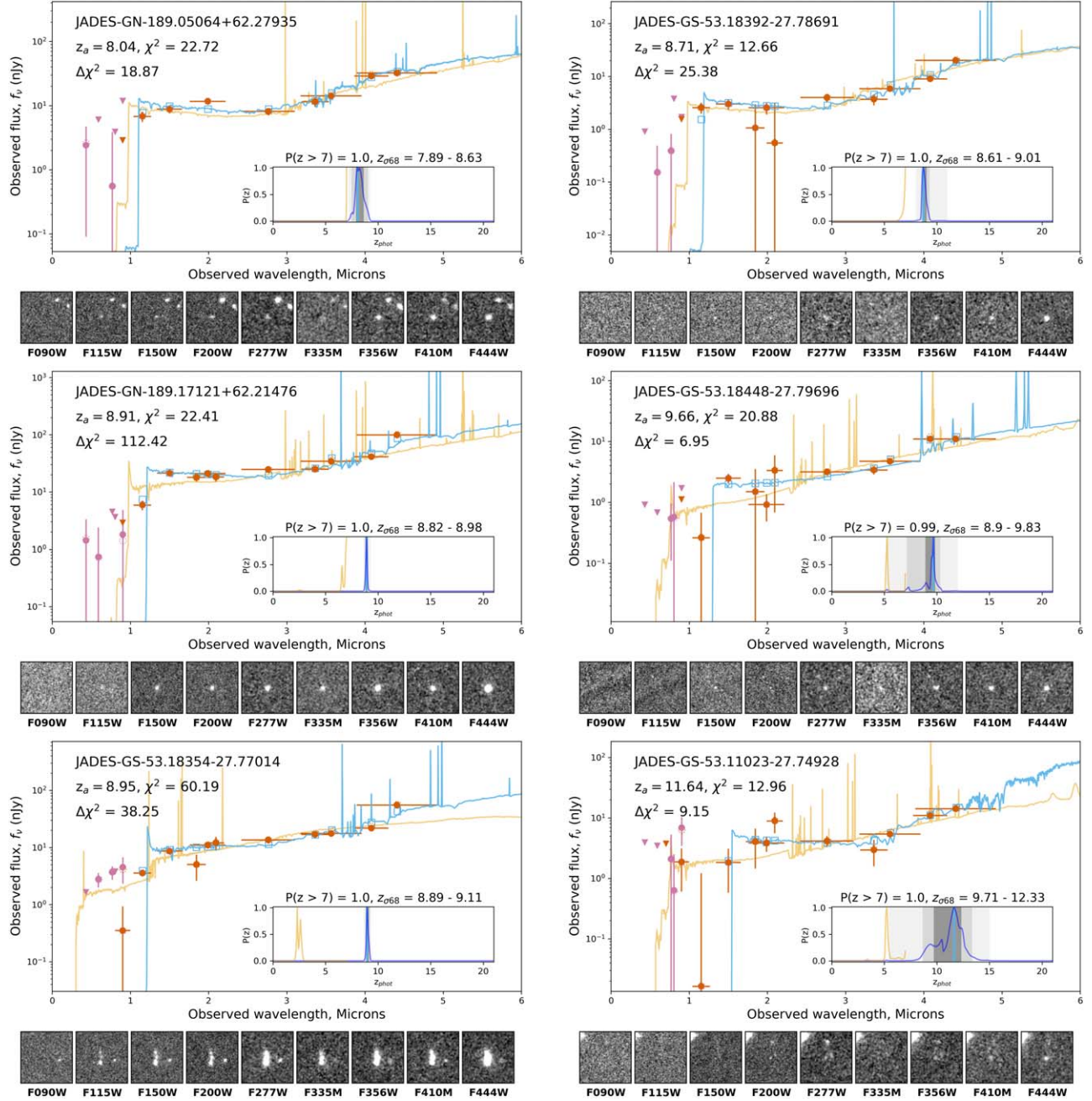Example Red Long-Wavelength Slope Candidates

Figure 15. Example SEDs for six candidate galaxies with red long-wavelength slopes. In each panel, the colors, lines, and symbols are as in Figure 2.

JADES sources at $z = 7-9$ with red long-wavelength slopes is discussed in R. Endsley et al. (2024, in preparation). However, until a number of these sources are followed up with deep spectroscopy, their nature will remain elusive.

6. Conclusions

In this paper, we have assembled a sample of 717 galaxies and candidate galaxies at $z > 8$ selected from the 125 square arcmin JWST JADES observations of GOODS-N and GOODS-S. We combined these data with publicly available medium-band observations from JEMS and FRESCO, and describe our data reduction and photometric extraction. Our primary results are listed below:

1. Using the template-fitting code EAZY, we calculated photometric redshifts for the JADES sources, and selected $z > 8$ candidates based on source S/N, the resulting probability of the galaxy being at $z > 7$, $P(z > 7)$, and the difference in χ^2 between the best fit at $z > 8$ and the fit at $z < 7$. The final sample was visually inspected by seven of the authors, and contains 182 objects in GOODS-N and 535 objects in GOODS-S, consistent with the areas and observational depths in the different portions of the JADES survey.

Table 6
Additional $z > 8$ Candidates from EAZY Template Fits

	Photometric Redshifts (Larson et al. 2023 Templates)						Photometric Redshifts (This Study)					
JADES ID	EAZY z_a	$\chi^2_{\min}$	$z_{\sigma68,\mathrm{low}}$	$z_{\sigma68,\mathrm{high}}$	$P(z > 7)$	$\Delta\chi^2$	EAZY z_a	$\chi^2_{\min}$	$z_{\sigma68,\mathrm{low}}$	$z_{\sigma68,\mathrm{high}}$	$P(z > 7)$	$\Delta\chi^2$
JADES-GS-53.05706-27.81652	8.92	13.72	8.54	10.01	0.984	6.190	1.89	15.14	2.14	10.25	0.793	0.0
JADES-GS-53.1153-27.80992	8.52	6.16	7.42	8.99	0.935	4.108	7.39	6.45	7.36	9.55	0.915	3.226
JADES-GS-53.13383-27.82825	8.02	13.13	7.58	8.09	1.000	16.976	7.89	10.72	7.72	7.98	1.000	32.386
JADES-GS-53.14036-27.79026	8.61	20.72	8.28	8.77	0.979	5.167	6.99	23.51	7.01	8.69	0.859	0.0
JADES-GS-53.14712-27.77639	8.14	18.44	8.04	8.30	0.876	5.791	8.30	20.71	6.06	8.44	0.691	2.222
JADES-GS-53.14992-27.88179	8.94	26.30	8.14	8.95	0.919	4.484	8.96	25.67	2.42	8.98	0.678	2.254
JADES-GS-53.18389-27.82345	8.20	15.47	7.90	8.38	1.000	20.058	1.83	20.18	1.84	8.28	0.578	0.0
JADES-GN-189.07044+62.29257	8.34	23.40	7.50	8.45	1.000	12.288	7.20	15.42	7.17	8.22	1.000	12.651
JADES-GN-189.26946+62.19909	8.11	13.93	7.60	8.29	0.997	7.348	7.84	15.67	7.40	8.12	0.995	5.804
JADES-GN-189.29444+62.14231	8.79	16.89	8.16	9.00	0.984	7.340	1.86	18.56	1.85	8.79	0.499	0.0

2. The photometric redshifts of these sources extend to $z \sim 18$, with an F277W Kron magnitude range of 25–31 (AB). The brightest source in our sample is the previously studied galaxy GN-z11 ($m_{\mathrm{F277W,Kron}} = 25.73$). We find 33 galaxy candidates at $z_a > 12$, with the highest-redshift candidate being JADES-GN-189.15981+62.28898 with a photometric redshift of $z_a = 18.79$.

3. We find a number galaxies and galaxy candidates at $z = 8$ -12 that are visually extended across many kiloparsecs and consist of multiple UV-bright clumps with underlying diffuse optical emission, potentially demonstrating very early massive galaxy growth.

4. Forty-two of the sources in our sample have spectroscopic redshift measurements. Each spectroscopic redshift agrees with the photometric redshift for the source within $|z_{\mathrm{spec}} - z_a|/(1 + z_{\mathrm{spec}}) < 0.15$. We find an average offset between the calculated photometric redshifts and the spectroscopic redshifts of $\langle \Delta z = z_{\mathrm{spec}} - z_a \rangle = 0.26$, lower than the results seen with other high-redshift samples in the literature. We speculate that the offset may be due to differences between the templates used to fit these objects and the observed galaxy SEDs, which will be mitigated as more accurate templates are created using high-redshift galaxy spectra from JWST/NIRSpec.

5. To explore whether any of the sources are consistent with being low-mass stars, we fit our sources with brown-dwarf models and measure whether the objects are unresolved. The galaxy templates fit the photometry with better accuracy than the brown-dwarf templates for the vast majority of cases.

6. We demonstrate that while traditional color selection would find most of the sources in our sample, at specific redshift ranges there are a number of sources that fall outside of typical color-selection criteria.

7. These results are robust to the exact EAZY templates used; the vast majority of sources found in our sample have similar redshifts when fit using the independently derived templates from Larson et al. (2023).

8. Our sample includes a number of intriguing sources with red long-wavelength slopes, potentially from dust heated by a growing supermassive black hole at $z > 8$. This red slope could also be due to an abundance of strong optical line emission from young stellar populations.

Taken together, these sources represent an exciting and robust sample for follow-up studies of the early Universe. The detailed stellar populations, as well as the resulting evolution of the mass and luminosity functions for the $z > 8$ JADES galaxies, will be found in forthcoming studies from the JADES collaboration members. We also look forward to JADES Cycle 2 observations, which will push to fainter observed fluxes. In addition, many of these sources will be observed with JADES NIRSpec micro-shutter assembly spectroscopy to both confirm their redshifts and to explore their ionization and metallicity properties. JWST has only just opened the door to the early Universe, and the years to come promise to be the most scientifically fruitful in the history of extragalactic science.

Appendix A
Exploring the Origin of Photometric Redshift Gaps At $z \sim 10$ and $z \sim 13$

In Figure 4, we plot the photometric redshift distribution of the $z > 8$ candidates, and note in Section 4 that there are relative gaps in the distribution at $z \sim 10$ and $z \sim 13$. As
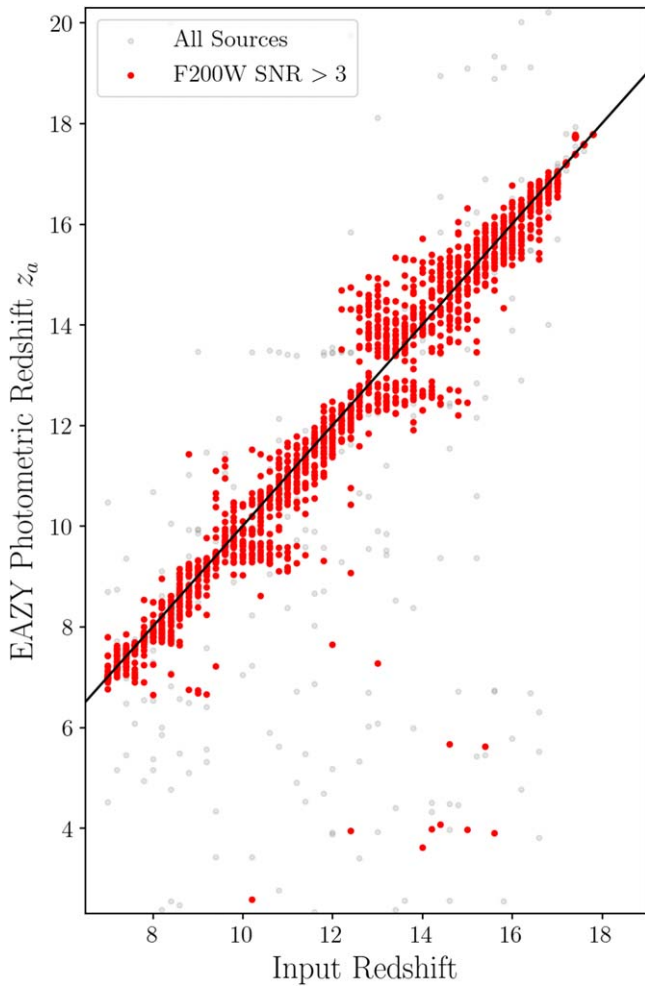
Figure 16. Photometric redshifts plotted against input redshifts for a simulated EAZY SED placed at a grid of uniformly spaced redshifts between $z = 7$ and 18 with $\Delta z = 0.2$, and at F200W S/N values between 0.5 and 20. We plot all of the resulting photometric redshifts in gray, and those with F200W S/N > 3 in red. We see a pileup of sources at photometric redshifts of $z \sim 10$ and $z \sim 13$.

Figure 17. Distribution of photometric redshifts from the results shown in Figure 16. We plot the distribution of all of the sources with gray bars, and we plot the distribution of sources with F200W S/N > 3 with red bars. The gaps we observe at $z \sim 10$ and $z \sim 13$ in Figure 4 are more easily visible here for the simulated galaxies.

mentioned in this section, these gaps arise due to the usage of wide NIRCam F090W, F115W, and F150W filters to estimate redshifts. To help explore this effect, we calculated photometric redshifts using the same EAZY fitting procedure described in the text but for a simulated SED placed at known redshifts. We started with the best-fit SED from EAZY for a bright source in our sample and artificially redshifted this SED to between $z = 7$ and 18 with $\Delta z = 0.2$. We calculated the photometry for the SED at these redshifts with our JADES filter set, and added
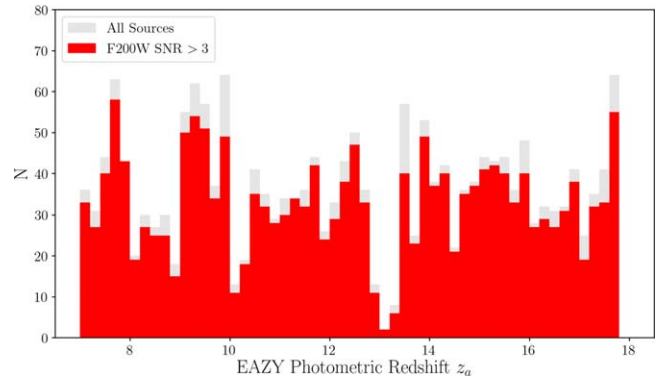
Gaussian noise in agreement with the values presented in Table 1 for the JADES Deep footprint, with a uniform grid of F200W S/N values between 0.5 and 20 and ΔS/N = 0.5. We then fit the noisy photometry for these artificial sources using the same EAZY templates and procedure as done on the full sample, and we plot the resulting photometric redshifts against the input redshifts in Figure 16. In Figure 17, we plot the photometric redshift distribution from the EAZY fits. In each figure, we plot sources at all S/N values in light gray, and those sources with F200W S/N > 3 in red.

We observe the same gaps in the photometric redshifts for these simulated source fits as are seen for the true galaxies in Figure 4. The gaps are more easily visible in the simulated plots due to the uniform distribution of the input redshifts. There is a pileup of sources at redshifts just lower than each observed gap, comprised of objects at higher simulated spectroscopic redshift, but where the Lyα break falls between two adjacent filters such that photometrically they are not distinguishable from a galaxy at slightly lower redshift.

Appendix B
Additional Tables and Figures

In Figures 18, 19, and 20, we plot the additional candidate galaxies in our sample at $z_a > 12$ continued from Figure 8 and with colors, lines, and symbols as in Figure 2. In Table 6, we provide additional $z > 8$ candidates derived using the Larson et al. (2023) EAZY templates, as discussed in Section 4.8.
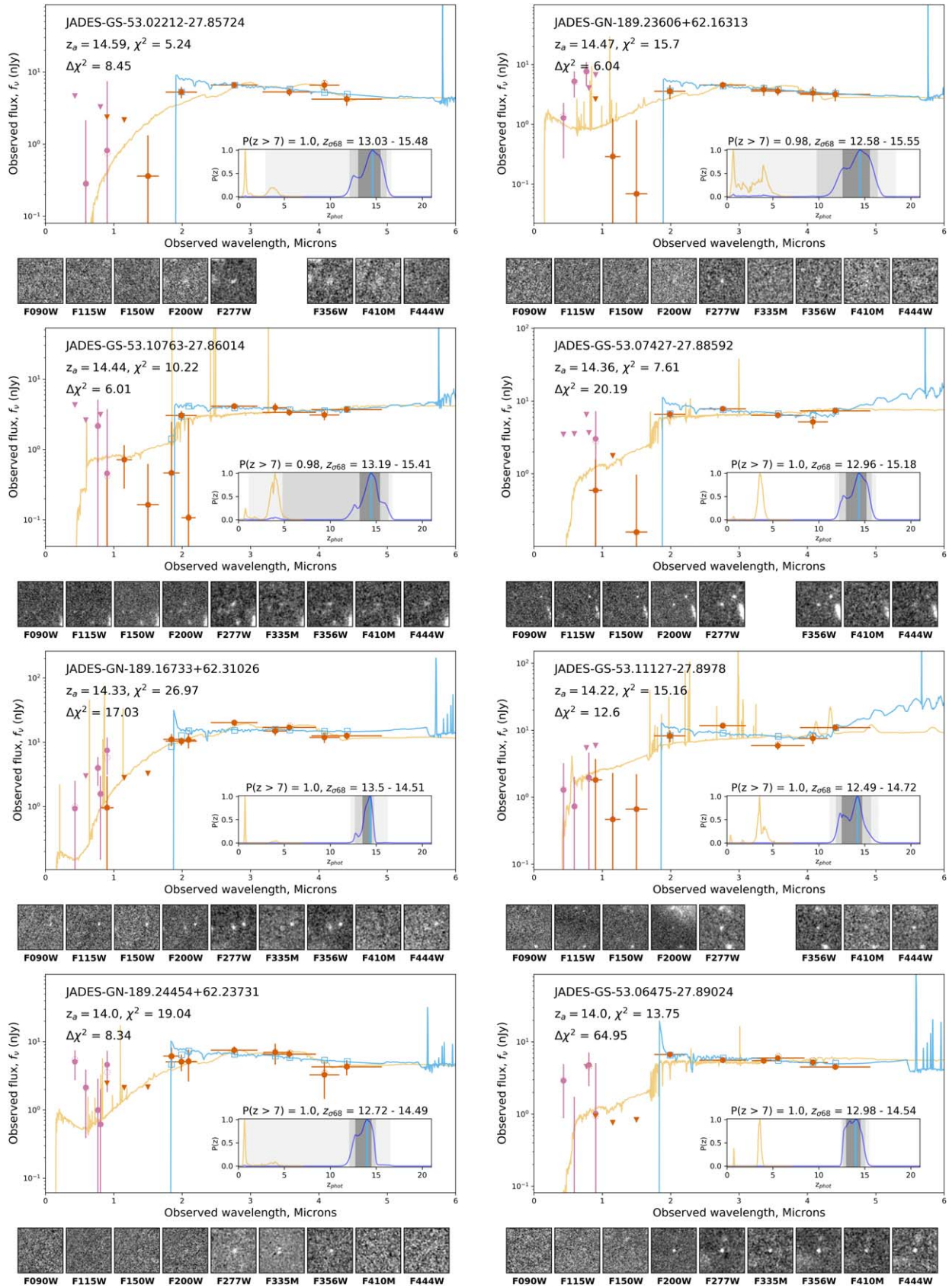
$z > 12$ Candidates, Part II

Figure 18. Continuation of Figure 8. In each panel, the colors, lines, and symbols are as in Figure 2.
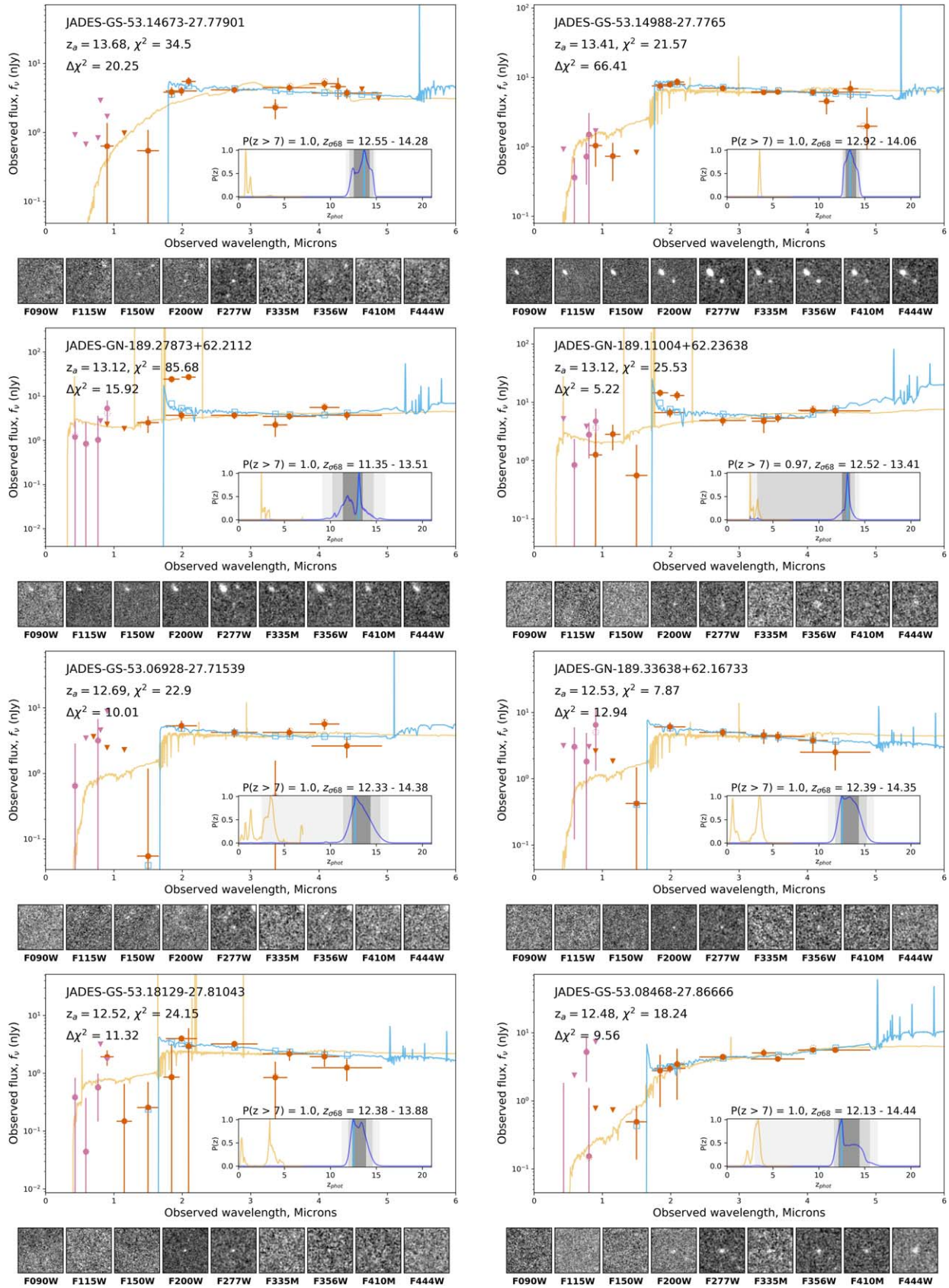
$z > 12$ Candidates, Part III

Figure 19. Continuation of Figure 18. In each panel, the colors, lines, and symbols are as in Figure 2.
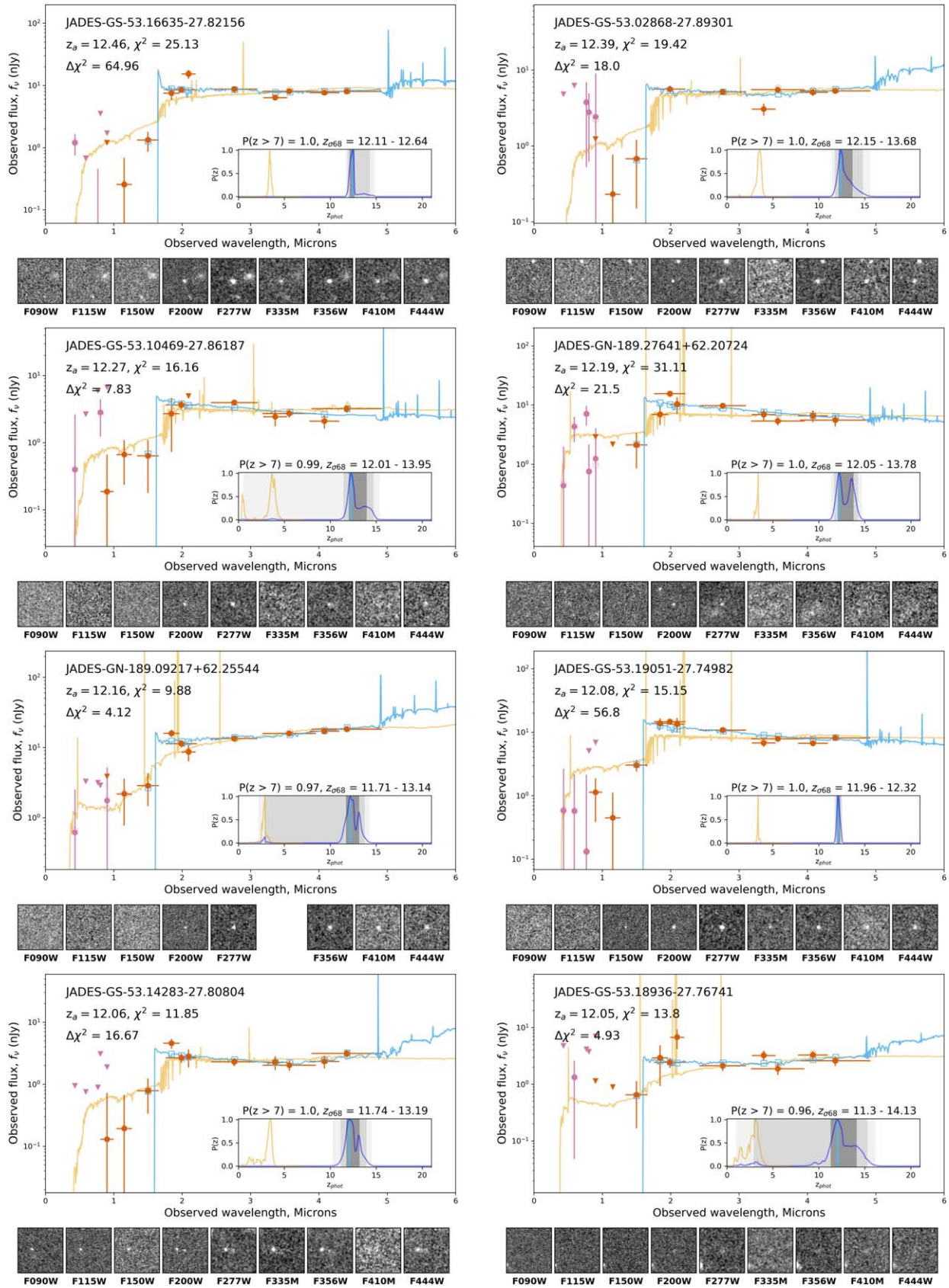
$z > 12$ Candidates, Part IV

Figure 20. Continuation of Figure 19. In each panel, the colors, lines, and symbols are as in Figure 2.

ORCID iDs

Kevin N. Hainline ⓘ https://orcid.org/0000-0003-4565-8239
Benjamin D. Johnson ⓘ https://orcid.org/0000-0002-9280-7594
Brant Robertson ⓘ https://orcid.org/0000-0002-4271-0364
Sandro Tacchella ⓘ https://orcid.org/0000-0002-8224-4505
Jakob M. Helton ⓘ https://orcid.org/0000-0003-4337-6211
Fengwu Sun ⓘ https://orcid.org/0000-0002-4622-6617
Daniel J. Eisenstein ⓘ https://orcid.org/0000-0002-2929-3121
Charlotte Simmonds ⓘ https://orcid.org/0000-0003-4770-7516
Michael W. Topping ⓘ https://orcid.org/0000-0001-8426-1141
Lily Whitler ⓘ https://orcid.org/0000-0003-1432-7744
Christopher N. A. Willmer ⓘ https://orcid.org/0000-0001-9262-9997
Marcia Rieke ⓘ https://orcid.org/0000-0002-7893-6170
Katherine A. Suess ⓘ https://orcid.org/0000-0002-1714-1905
Raphael E. Hviding ⓘ https://orcid.org/0000-0002-4684-9005
Alex J. Cameron ⓘ https://orcid.org/0000-0002-0450-7306
Stacey Alberts ⓘ https://orcid.org/0000-0002-8909-8782
William M. Baker ⓘ https://orcid.org/0000-0003-0215-1104
Stefi Baum ⓘ https://orcid.org/0000-0002-4735-8224
Rachana Bhatawdekar ⓘ https://orcid.org/0000-0003-0883-2226
Nina Bonaventura ⓘ https://orcid.org/0000-0001-8470-7094
Kristan Boyett ⓘ https://orcid.org/0000-0003-4109-304X
Andrew J. Bunker ⓘ https://orcid.org/0000-0002-8651-9879
Stefano Carniani ⓘ https://orcid.org/0000-0002-6719-380X
Stephane Charlot ⓘ https://orcid.org/0000-0003-3458-2275
Jacopo Chevallard ⓘ https://orcid.org/0000-0002-7636-0534
Zuyi Chen ⓘ https://orcid.org/0000-0002-2178-5471
Mirko Curti ⓘ https://orcid.org/0000-0002-2678-2560
Emma Curtis-Lake ⓘ https://orcid.org/0000-0002-9551-0534
Francesco D'Eugenio ⓘ https://orcid.org/0000-0003-2388-8172
Eiichi Egami ⓘ https://orcid.org/0000-0003-1344-9475
Ryan Endsley ⓘ https://orcid.org/0000-0003-4564-2771
Ryan Hausen ⓘ https://orcid.org/0000-0002-8543-761X
Zhiyuan Ji ⓘ https://orcid.org/0000-0001-7673-2257
Tobias J. Looser ⓘ https://orcid.org/0000-0002-3642-2446
Jianwei Lyu ⓘ https://orcid.org/0000-0002-6221-1829
Roberto Maiolino ⓘ https://orcid.org/0000-0002-4985-3819
Erica Nelson ⓘ https://orcid.org/0000-0002-7524-374X
Dávid Puskás ⓘ https://orcid.org/0000-0001-8630-2031
Tim Rawle ⓘ https://orcid.org/0000-0002-7028-5588
Lester Sandles ⓘ https://orcid.org/0000-0001-9276-7062
Aayush Saxena ⓘ https://orcid.org/0000-0001-5333-9970
Renske Smit ⓘ https://orcid.org/0000-0001-8034-7802
Daniel P. Stark ⓘ https://orcid.org/0000-0001-6106-5172
Christina C. Williams ⓘ https://orcid.org/0000-0003-2919-7495
Chris Willott ⓘ https://orcid.org/0000-0002-4201-7367
Joris Witstok ⓘ https://orcid.org/0000-0002-7595-121X

References

Adams, N. J., Conselice, C. J., Ferreira, L., et al. 2023, MNRAS, 518, 4755
Akins, H. B., Casey, C. M., Allen, N., et al. 2023, ApJ, 956, 61
Arrabal Haro, P., Dickinson, M., Finkelstein, S. L., et al. 2023a, Natur, 622, 707
Arrabal Haro, P., Dickinson, M., Finkelstein, S. L., et al. 2023b, ApJL, 951, L22
Astropy Collaboration, Price-Whelan, A. M., Sipőcz, B. M., et al. 2018, AJ, 156, 123
Astropy Collaboration, Robitaille, T. P., Tollerud, E. J., et al. 2013, A&A, 558, A33
Atek, H., Chemerynska, I., Wang, B., et al. 2023, MNRAS, 524, 5486
Austin, D., Adams, N., Conselice, C. J., et al. 2023, ApJL, 952, L7
Bagley, M. B., Finkelstein, S. L., Koekemoer, A. M., et al. 2023, ApJL, 946, L12
Bagley, M. B., Finkelstein, S. L., Rojas-Ruiz, S., et al. 2024, ApJ, 961, 209
Barkana, R., & Loeb, A. 2001, PhR, 349, 125
Barro, G., Perez-Gonzalez, P. G., Kocevski, D. D., et al. 2023, arXiv:2305.14418
Beckwith, S. V. W., Stiavelli, M., Koekemoer, A. M., et al. 2006, AJ, 132, 1729
Birrer, S., & Amara, A. 2018, PDU, 22, 189
Birrer, S., Shajib, A. J., Gilman, D., et al. 2021, JOSS, 6, 3283
Bolzonella, M., Miralles, J. M., & Pelló, R. 2000, A&A, 363, 476
Bonzini, M., Mainieri, V., Padovani, P., et al. 2012, ApJS, 203, 15
Bouwens, R. J., Illingworth, G., Ellis, R. S., et al. 2022, ApJ, 931, 81
Bouwens, R. J., Illingworth, G. D., González, V., et al. 2010, ApJ, 725, 1587
Bouwens, R. J., Illingworth, G. D., Labbe, I., et al. 2011a, Natur, 469, 504
Bouwens, R. J., Illingworth, G. D., Oesch, P. A., et al. 2011b, ApJ, 737, 90
Bouwens, R. J., Illingworth, G. D., Oesch, P. A., et al. 2015, ApJ, 803, 34
Bouwens, R. J., Oesch, P. A., Labbé, I., et al. 2016, ApJ, 830, 67
Bouwens, R. J., Oesch, P. A., Stefanon, M., et al. 2021, AJ, 162, 47
Bouwens, R. J., Stefanon, M., Brammer, G., et al. 2023, MNRAS, 523, 1036
Bouwens, R. J., Stefanon, M., Oesch, P. A., et al. 2019, ApJ, 880, 25
Bowler, R. A. A., Jarvis, M. J., Dunlop, J. S., et al. 2020, MNRAS, 493, 2059
Boyer, M. L., Anderson, J., Gennaro, M., et al. 2022, RNAAS, 6, 191
Bradley, L., Sipőcz, B., Robitaille, T., et al. 2023, astropy/photutils: v1.7.0, Zenodo, doi:10.5281/zenodo.7804137
Brammer, G. B., van Dokkum, P. G., & Coppi, P. 2008, ApJ, 686, 1503
Bridge, J. S., Holwerda, B. W., Stefanon, M., et al. 2019, ApJ, 882, 42
Bunker, A., & Wilkins, S. 2009, arXiv:0912.1351
Bunker, A. J., Saxena, A., Cameron, A. J., et al. 2023a, A&A, 677, A88
Bunker, A. J., Stanway, E. R., Ellis, R. S., & McMahon, R. G. 2004, MNRAS, 355, 374
Bunker, A. J., Wilkins, S., Ellis, R. S., et al. 2010, MNRAS, 409, 855
Bunker, A., et al. 2023b, A&A, submitted, arXiv:2306.02467
Caballero, J. A., Burgasser, A. J., & Klement, R. 2008, A&A, 488, 181
Cameron, A. J., Saxena, A., Bunker, A. J., et al. 2023, A&A, 677, A115
Castellano, M., Fontana, A., Treu, T., et al. 2022, ApJL, 938, L15
Coe, D., Benítez, N., Sánchez, S. F., et al. 2006, AJ, 132, 926
Coe, D., Salmon, B., Bradač, M., et al. 2019, ApJ, 884, 85
Conroy, C., & Gunn, J. E., 2010 FSPS: Flexible Stellar Population Synthesis, Astrophysics Source Code Library, ascl:1010.043
Cooper, M. C., Yan, R., Dickinson, M., et al. 2012, MNRAS, 425, 2116
Curtis-Lake, E., Carniani, S., Cameron, A., et al. 2023, NatAs, 7, 622
Curtis-Lake, E., McLure, R. J., Dunlop, J. S., et al. 2016, MNRAS, 457, 440
Cutri, R. M., Wright, E. L., Conrow, T., et al. 2021, yCat, II/328
Dayal, P., & Ferrara, A. 2018, PhR, 780, 1
D'Eugenio, F., Maiolino, R., Carniani, S., et al. 2023, arXiv:2311.09908
Donnan, C. T., McLeod, D. J., McLure, R. J., et al. 2023, MNRAS, 520, 4554
Dunlop, J. S. 2013, in The First Galaxies, ed. T. Wiklind, B. Mobasher, & V. Bromm, Vol. 396 (Berlin: Springer), 223
Eisenstein, D. J., Johnson, B. D., Robertson, B., et al. 2023b, arXiv:2310.12340
Eisenstein, D. J., Willott, C., Alberts, S., et al. 2023a, arXiv:2306.02465
Eldridge, J. J., Stanway, E. R., Xiao, L., et al. 2017, PASA, 34, e058
Ellis, R. S., McLure, R. J., Dunlop, J. S., et al. 2013, ApJL, 763, L7
Endsley, R., Stark, D. P., Whitler, L., et al. 2023, MNRAS, 524, 2312
Erb, D. K., Pettini, M., Shapley, A. E., et al. 2010, ApJ, 719, 1168
Ferland, G. J., Chatzikos, M., Guzmán, F., et al. 2017, RMxAA, 53, 385
Finkelstein, S. L., Bagley, M. B., Ferguson, H. C., et al. 2023, ApJL, 946, L13
Finkelstein, S. L., D'Aloisio, A., Paardekooper, J.-P., et al. 2019, ApJ, 879, 36
Finkelstein, S. L., Ryan, R. E. J., Papovich, C., et al. 2015, ApJ, 810, 71
Furtak, L. J., Zitrin, A., Plat, A., et al. 2023, ApJ, 952, 142
Gaia Collaboration, Brown, A. G. A., Vallenari, A., et al. 2021, A&A, 649, A1
Giavalisco, M. 2002, ARA&A, 40, 579
Giavalisco, M., Ferguson, H. C., Koekemoer, A. M., et al. 2004, ApJL, 600, L93
Grogin, N. A., Kocevski, D. D., Faber, S. M., et al. 2011, ApJS, 197, 35
Guhathakurta, P., Tyson, J. A., & Majewski, S. R. 1990, ApJL, 357, L9
Gwyn, S. D. J., & Hartwick, F. D. A. 1996, ApJL, 468, L77
Hainline, K. N., Helton, J. M., & Johnson, B. D. 2023, arXiv:2309.03250
Hainline, K. N., Hviding, R. E., Rieke, M., et al. 2020, ApJ, 892, 125
Harikane, Y., Inoue, A. K., Mawatari, K., et al. 2022, ApJ, 929, 1

Harikane, Y., Ouchi, M., Oguri, M., et al. 2023, ApJS, 265, 5
Harikane, Y., Ouchi, M., Ono, Y., et al. 2016, ApJ, 821, 123
Harris, C. R., Millman, K. J., van der Walt, S. J., et al. 2020, Natur, 585, 357
Helton, J. M., Sun, F., Woodrum, C., et al. 2024, ApJ, 962, 124
Horne, K. 1986, PASP, 98, 609
Hunter, J. D. 2007, CSE, 9, 90
Illingworth, G., Magee, D., Bouwens, R., et al. 2016, arXiv:1606.00841
Illingworth, G. D., Magee, D., Oesch, P. A., et al. 2013, ApJS, 209, 6
Ishigaki, M., Kawamata, R., Ouchi, M., et al. 2015, ApJ, 799, 12
Jakobsen, P., Ferruit, P., Alves de Oliveira, C., et al. 2022, A&A, 661, A80
Johnson, B. D., Leja, J., Conroy, C., & Speagle, J. S. 2021, ApJS, 254, 22
Kashino, D., Lilly, S. J., Matthee, J., et al. 2023, ApJ, 950, 66
Koekemoer, A. M., Ellis, R. S., McLure, R. J., et al. 2013, ApJS, 209, 3
Koekemoer, A. M., Faber, S. M., Ferguson, H. C., et al. 2011, ApJS, 197, 36
Koo, D. C. 1985, AJ, 90, 418
Koo, D. C. 1999, in ASP Conf. Ser. 191, Photometric Redshifts and the
    Detection of High Redshift Galaxies, ed. R. Weymann et al. (San Francisco,
    CA: ASP), 3
Labbé, I., Huang, J., Franx, M., et al. 2005, ApJL, 624, L81
Labbé, I., van Dokkum, P., Nelson, E., et al. 2023, Natur, 616, 266
Lanzetta, K. M., Yahil, A., & Fernández-Soto, A. 1996, Natur, 381, 759
Larson, R. L., Hutchison, T. A., Bagley, M., et al. 2023, ApJ, 958, 141
Leethochawalit, N., Trenti, M., Santini, P., et al. 2023, ApJL, 942, L26
Leung, G. C. K., Bagley, M. B., Finkelstein, S. L., et al. 2023, ApJL, 954, L46
Lorenzoni, S., Bunker, A. J., Wilkins, S. M., et al. 2011, MNRAS, 414, 1455
Lorenzoni, S., Bunker, A. J., Wilkins, S. M., et al. 2013, MNRAS, 429, 150
Lotz, J. M., Koekemoer, A., Coe, D., et al. 2017, ApJ, 837, 97
Madau, P. 1995, ApJ, 441, 18
Madau, P., Ferguson, H. C., Dickinson, M. E., et al. 1996, MNRAS, 283, 1388
Marley, M., Saumon, D., Morley, C., & Fortney, J. 2018, Sonora 2018: Cloud-
    free, solar composition, solar C/O substellar atmosphere models and
    spectra, nc_m+0.0_co1.0_v1.0, v1 Zenodo, doi:10.5281/zenodo.1309035
McLeod, D. J., McLure, R. J., & Dunlop, J. S. 2016, MNRAS, 459, 3812
McLure, R. J., Dunlop, J. S., Bowler, R. A. A., et al. 2013, MNRAS, 432, 2696
Meisner, A. M., Faherty, J. K., Kirkpatrick, J. D., et al. 2020, ApJ, 899, 123
Momcheva, I. G., Brammer, G. B., van Dokkum, P. G., et al. 2016, ApJS,
    225, 27
Morishita, T., Roberts-Borsani, G., Treu, T., et al. 2023, ApJL, 947, L24
Morishita, T., Trenti, M., Stiavelli, M., et al. 2018, ApJ, 867, 150
Naidu, R. P., Oesch, P. A., Setton, D. J., et al. 2022, arXiv:2208.02794
Nonino, M., Glazebrook, K., Burgasser, A. J., et al. 2023, ApJL, 942, L29
Oesch, P. A., Bouwens, R. J., Illingworth, G. D., Labbé, I., & Stefanon, M.
    2018, ApJ, 855, 105
Oesch, P. A., Bouwens, R. J., Illingworth, G. D., et al. 2013, ApJ, 773, 75
Oesch, P. A., Bouwens, R. J., Illingworth, G. D., et al. 2014, ApJ, 786, 108
Oesch, P. A., Brammer, G., Naidu, R. P., et al. 2023, MNRAS, 525, 2864
Oesch, P. A., Brammer, G., van Dokkum, P. G., et al. 2016, ApJ, 819, 129

Oke, J. B. 1974, ApJS, 27, 21
Oke, J. B., & Gunn, J. E. 1983, ApJ, 266, 713
Ouchi, M., Ono, Y., & Shibuya, T. 2020, ARA&A, 58, 617
Pello, R., Miralles, J. M., Le Borgne, J. F., et al. 1996, A&A, 314, 73
Pérez-González, P. G., Costantin, L., Langeroodi, D., et al. 2023, ApJL,
    951, L1
Planck Collaboration, Aghanim, N., Akrami, Y., et al. 2020, A&A, 641, A6
Postman, M., Coe, D., Benítez, N., et al. 2012, ApJS, 199, 25
Prada, F., Behroozi, P., Ishiyama, T., Klypin, A., & Pérez, E. 2023,
    arXiv:2304.11911
Quadri, R., Marchesini, D., van Dokkum, P., et al. 2007, AJ, 134, 1103
Reddy, N. A., Steidel, C. C., Erb, D. K., Shapley, A. E., & Pettini, M. 2006,
    ApJ, 653, 1004
Rieke, M. & Jades Collaboration 2023, BAAS, 55, 177.55
Rieke, M. J., Kelly, D., & Horner, S. 2005, Proc. SPIE, 5904, 1
Rigby, J., Perrin, M., McElwain, M., et al. 2023, PASP, 135, 048001
Robertson, B., Johnson, B. D., Tacchella, S., et al. 2023, arXiv:2312.10033
Robertson, B. E., Tacchella, S., Johnson, B. D., et al. 2023, NatAs, 7, 611
Rojas-Ruiz, S., Finkelstein, S. L., Bagley, M. B., et al. 2020, ApJ, 891, 146
Ryan, R. E. J., Hathi, N. P., Cohen, S. H., & Windhorst, R. A. 2005, ApJL,
    631, L159
Ryan, R. E. J., & Reid, I. N. 2016, AJ, 151, 92
Schenker, M. A., Robertson, B. E., Ellis, R. S., et al. 2013, ApJ, 768, 196
Schlawin, E., Leisenring, J., Misselt, K., et al. 2020, AJ, 160, 231
Scoville, N., Aussel, H., Brusa, M., et al. 2007, ApJS, 172, 1
Shibuya, T., Ouchi, M., & Harikane, Y. 2015, ApJS, 219, 15
Stark, D. P. 2016, ARA&A, 54, 761
Steidel, C. C., & Hamilton, D. 1992, AJ, 104, 941
Stern, D., & Spinrad, H. 1999, PASP, 111, 1475
Sun, F., Egami, E., Pirzkal, N., et al. 2023, ApJ, 953, 53
Tacchella, S., Eisenstein, D. J., Hainline, K., et al. 2023, ApJ, 952, 74
Teplitz, H. I., Rafelski, M., Kurczynski, P., et al. 2013, AJ, 146, 159
Topping, M. W., Stark, D. P., Endsley, R., et al. 2022, ApJ, 941, 153
Trenti, M., Bradley, L. D., Stiavelli, M., et al. 2011, ApJL, 727, L39
Virtanen, P., Gommers, R., Oliphant, T. E., et al. 2020, NatMe, 17, 261
Weisz, D. R., McQuinn, K. B. W., Savino, A., et al. 2023, ApJS, 268, 15
Whitaker, K. E., Ashas, M., Illingworth, G., et al. 2019, ApJS, 244, 16
Whitaker, K. E., Labbé, I., van Dokkum, P. G., et al. 2011, ApJ, 735, 86
Whitler, L., Endsley, R., Stark, D. P., et al. 2023, MNRAS, 519, 157
Wilkins, S. M., Stanway, E. R., & Bremer, M. N. 2014, MNRAS, 439, 1038
Williams, C. C., Alberts, S., Ji, Z., et al. 2023a, arXiv:2311.07483
Williams, C. C., Curtis-Lake, E., Hainline, K. N., et al. 2018, ApJS, 236, 33
Williams, C. C., Tacchella, S., Maseda, M. V., et al. 2023b, ApJS, 268, 64
Williams, R. E., Blacker, B., Dickinson, M., et al. 1996, AJ, 112, 1335
Yan, H., Ma, Z., Ling, C., Cheng, C., & Huang, J.-S. 2023, ApJL, 942, L9
Yan, H.-J., Windhorst, R. A., Hathi, N. P., et al. 2010, RAA, 10, 867
Zavala, J. A., Buat, V., Casey, C. M., et al. 2023, ApJL, 943, L9